How resistive must grain boundaries in polycrystalline superconductors be, to limit J_c?

You may also be interested in:

The critical current density of grain boundary channels in polycrystalline HTS and LTS superconductors in magnetic fields
P Sunwong, J S Higgins, Y Tsui et al.

Theory of RF superconductivity for resonant cavities
Alex Gurevich

Exploration of new superconductors and functional materials, and fabrication of superconducting tapes and wires of iron pnictides
Hideo Hosono, Keiichi Tanabe, Eiji Takayama-Muromachi et al.

Current distributions inhigh-{T}c superconductors
Ch Jooss, J Albrecht, H Kuhn et al.

Thin film growth of Fe-based superconductors: from fundamental properties to functional devices. A comparative review
S Haindl, M Kidszun, S Oswald et al.

The behavior of grain boundaries in the Fe-based superconductors
J H Durrell, C-B Eom, A Gurevich et al.

Weak links in high critical temperature superconductors
Francesco Tafuri and John R Kirtley

Mechanism of vortex motion in high-temperature superconductors
Roger Wördenweber

How resistive must grain boundaries in polycrystalline superconductors be, to limit J_c?

Guanmei Wang, Mark J Raine and Damian P Hampshire

Durham University, Department of Physics, Superconductivity Group, South Road, Durham, DH1 3LE, United Kingdom

E-mail: guanmei.wang@durham.ac.uk

CrossMark

Abstract

Although we can use misorientation angle to distinguish the grain boundaries that can carry high critical current density (J_c) in high temperature superconductors (HTS) from those that cannot, there is no established normal state property equivalent. In this paper, we explore the superconducting and normal state properties of the grains and grain boundaries of polycrystalline $YBa_2Cu_3O_{7-x}$ (YBCO) using complementary magnetisation and transport measurements, and calculate how resistive grain boundaries must be to limit J_c in polycrystalline superconductors. The average resistivity of the grain boundaries, ρ_{GB}, in our micro- and nanocrystalline YBCO are $0.12\,\Omega m$ and $8.2\,\Omega m$, values which are much higher than that of the grains (ρ_G) and leads to huge ρ_{GB}/ρ_G values of 2×10^3 and 1.6×10^5 respectively. We find that the grain boundaries in our polycrystalline YBCO are sufficiently resistive that we can expect the transport J_c to be several tens of orders of magnitude below the potential current density of the grains in our YBCO samples, as is found experimentally. Calculations presented show that increasing J_c values by $\sim$2 orders of magnitude in high fields is still possible in all state-of-the-art technological high-field superconductors. We conclude: grain boundary engineering is unlikely to improve J_c sufficiently in randomly aligned polycrystalline YBCO, to make it technologically useful for high-field applications; in low temperature superconducting intermetallics, such as Nb_3Sn, large increases in J_c may be achieved by completely removing the grain boundaries from these materials and, as is the case for thin films of Nb, $Ba(FeCo)_2As_2$ and HTS materials, by incorporating additional artificial pinning.

Keywords: superconductivity, critical current, bulk YBCO, nanocrystalline

(Some figures may appear in colour only in the online journal)

1. Introduction

The applied superconductivity research community is always trying to increase the critical current density ($J_c(B, T)$) of superconducting materials. There are two quite distinct requirements for achieving high J_c in practical materials. The local depairing current density ($J_D(B, T)$), which is the theoretical limit associated with the density of Cooper pairs, must be high enough throughout the entire material, and the current density associated with local flux pinning ($J_P(B, T)$) must be sufficiently high to stop flux motion. Thereafter many other issues, such as the strain and/or irradiation tolerance of J_c, or the thermal stability of the conductor, become important depending on the application. But, in most applications, high J_c in high magnetic fields is usually the primary technological and economic driver.

In the historical development of the low temperature superconductor (LTS) Nb_3Sn, reducing the grain size in polycrystalline material, significantly increased J_c in high magnetic fields [1]. It was reasonable to assume that in such an intermetallic superconductor, smaller grain size increased

pinning and that the metallic bonding ensured that J_D was sufficiently high throughout the entire material that any depression in J_D in the grain boundaries was unimportant. However, over the last decade the progress in increasing J_c in Nb$_3$Sn has been relatively slow and the simple pinning approach that considers flux pinning alone (e.g. fluxons depinning themselves from isolated pinning sites) has not helped produced any further significant increases in J_c. More recent computational three-dimensional time-dependent-Ginzburg–Landau (TDGL) modelling [2] has shown that in polycrystalline superconductors, the dissipation mechanism can consist of fluxons moving along grain boundary channels past fluxons that are held stationary within the grains by strong surface pinning. The increase in pinning due to smaller grains is most likely caused by an increase in the density of triple points along the channels or by providing a more tortuous channel path along which the fluxons must flow. Hence, we suggest that in polycrystalline materials, it is useful to consider depairing and depinning separately and invoke separate values of J_D and J_P for both the grains and the grain boundary channels. This approach helps articulate the open question of whether further significant increases in J_c will be achieved, even in LTS polycrystalline materials, by increasing J_D or by increasing J_P along grain boundary channels. Since in practice we cannot completely decouple J_D and J_P and J_P cannot be larger than J_D, this approach becomes one of identifying whether or not J_D is sufficiently low (at the grain boundaries), that it is the barrier to achieving further increases in J_c.

In developing high temperature superconductors (HTS), the role of grain boundaries was found to be quite different to that of LTS [3, 4]. In the pioneering work of Dimos *et al* [3], J_c was measured in YBa$_2$Cu$_3$O$_{7-x}$ (YBCO) bicrystals for different geometries and was found to decrease exponentially with increasing misorientation angle. This led to research into repairing the grain boundaries such as doping them to improve oxygen content or carrier concentration, with a view to increasing J_c [5, 6]. Experimental work was also supported by computational studies which included modelling the flow of current through a grain boundary at an atomic level [7] and modelling grain boundaries, both analytically [8] and using TDGL theory [2, 9, 10]. Eventually, industry concluded that large-angle grain boundaries in HTS materials depressed J_c so severely that it committed itself to making kilometre-length pseudo single-crystal 2 G tapes of HTS [11] that were designed to completely exclude large-angle grain boundaries. In parallel with the development of 2 G tapes, the language of 'weak-links' was developed in the literature. It emphasised that although some materials have local regions of very high J_c, the practical limit for a material is usually determined by those regions of lowest J_c, although it does not make clear whether the 'weak-link' is because of low J_D or low J_P.

Understanding and improving grain boundaries in both LTS and HTS materials is important because despite the huge applied superconductivity research effort, J_c in most materials is still far from its maximum theoretical value—the depairing current density of the superconductor (J_{DSc}) [12]. The first panel in figure 1 shows the critical current density versus field

at 4.2 K in the superconducting layer of many of the most important high-field superconductors. There are other similar datasets in the literature, such as the excellent webpage produced and maintained by Lee [13]. Samples reported in figure 1 were chosen by prioritising datasets providing a broad range of magnetic field data, and the quality of samples and measurements. The second panel in figure 1 shows the data replotted as current density normalised by the depairing current density at zero field and 4.2 K ($J_c/J_{DSc}(0, 4.2)$), versus the applied magnetic field normalised by the upper critical field at 4.2 K ($B_{app}/B_{c2}(4.2)$). The temperature-dependent depairing current density in zero field has been calculated using

$$J_{DSc}(0, T) = \frac{\Phi_0}{3\sqrt{3}\,\pi\mu_0\lambda^2(T)\xi(T)}, \quad (1)$$
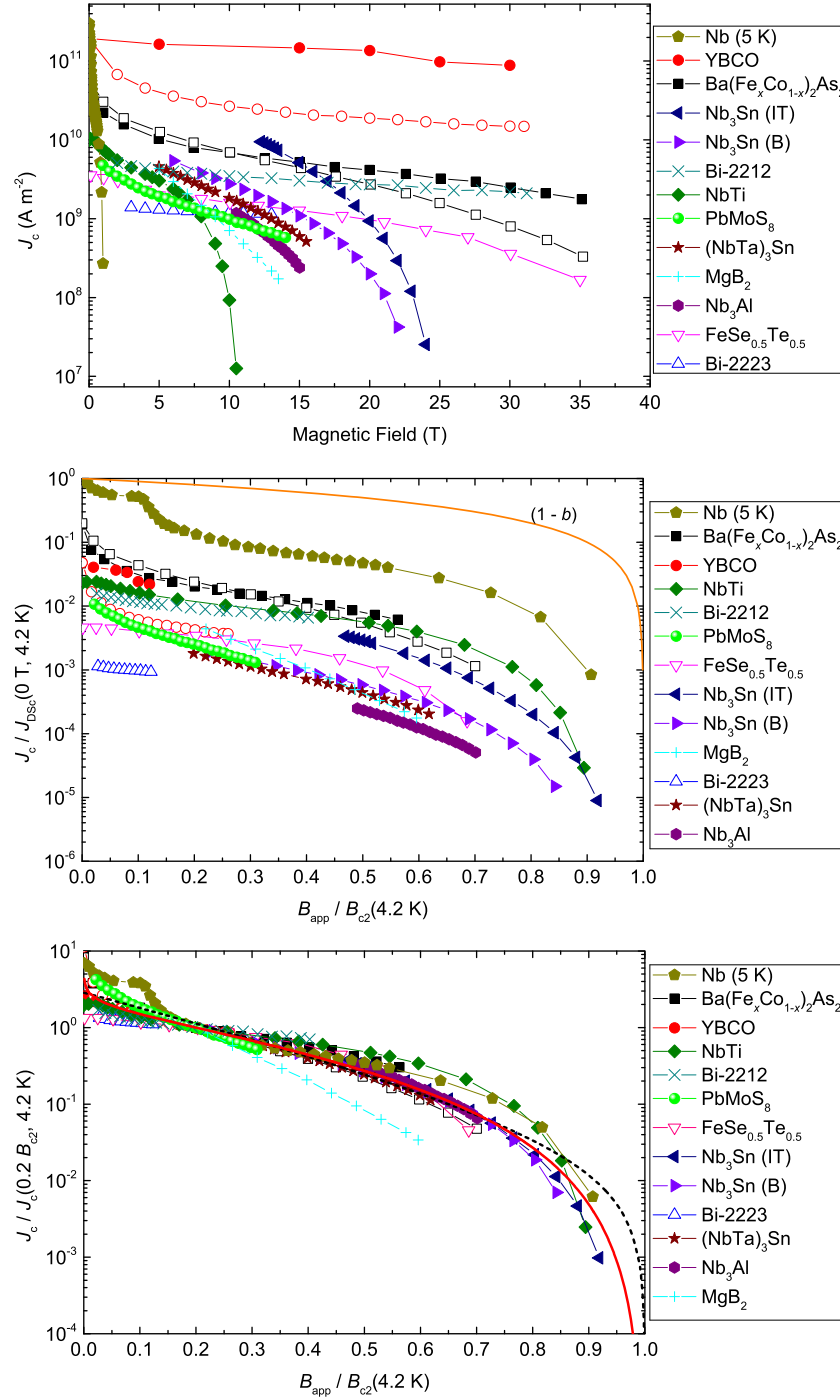
where for isotropic materials, Φ_0 is the flux quantum, $\lambda(T)$ is the Ginzburg–Landau (G–L) penetration depth and $\xi(T)$ is the G–L coherence length. The $(1 - b)$ curve shows the in-field theoretical limit derived from G–L theory where $J_{DSc}(B, 4.2) = J_{DSc}(0, 4.2)(1 - b)$, where $b = B_{app}/B_{c2}(4.2)$. The appendix provides the method used for calculating the depairing current density in anisotropic materials and table 1 lists the values of $J_{DSc}(0, 4.2)$ used to produce the second panel [13–25]. We note that for YBCO, Ba(FeCo)$_2$As$_2$ and FeSe$_{0.5}$Te$_{0.5}$, there are small differences in the values of $\xi_{ab}\lambda_{ab}$ and $\xi_c\lambda_c$, due to the fact that B_{c2} and B_{c1} (or λ) were measured by different groups on different samples. We have neglected the differences between the upper critical field and the irreversibility field, which are generally only important at high temperatures for the HTSs (typically when the υ values are low) [26–28]. The second panel in figure 1 shows that even in technologically mature materials such as NbTi, J_c values in high magnetic fields are still nearly two orders of magnitude below the theoretical upper limit of the depairing current density. The third panel in figure 1 shows J_c normalised to unity at $0.2B_{c2}$. One can globally fit these normalised data using the long-established standard flux pinning equation, of the form

$$F_P = J_c \times B = C\, b^p(1 - b)^q, \quad (2)$$

where $p = 0.82$ and $q = 2.4$. The values of p and q vary considerably from one material to another when fitted individually. For example for NbTi, $p = 1$ and $q = 1$, whereas for the A15 compounds, $p = 0.5$ and $q = 2$ [29]. Nevertheless, the panel shows that to first order, the in-field behaviour of J_c is not very different across this range of quite different superconducting materials. Equally the data are reasonably well parameterised by an equation used for high temperature superconducting materials of the form [8, 30]

$$J_c = \alpha\left(1 - \frac{B}{B_{c2}(T)}\right)\exp\left(-\frac{B}{\beta(T)}\right), \quad (3)$$

where at $T = 4.2$ K, $\alpha = 2.9$ and $\beta(4.2) = 0.28\, B_{c2}(4.2)$. Equation (2) suggests flux pinning is important whereas the exponential in equation (3) suggests the decay of the order parameter across the grain boundaries is important. Hence, although the physical processes associated with these two equations are completely different, it is clear that fitting the data

Figure 1. Upper panel: critical current density of the superconducting layer J_c as a function of applied magnetic field B_{app}. The J_c data for YBCO (Superpower 'Turbo' double layer tape), Bi-2212 (OST 2212 wire with 100 bar over-pressure) and Bi-2223 (Sumitomo Electric Industries 'DI' BSCCO tape) are taken from [28]. J_c data for Nb (thin film with artificial nanoscale pores) [12] (measured at 5 K), Nb–47Ti ([133], 37% superconductor cross-section area (SCSA)), Nb_3Sn (Internal Sn RRP (IT), 12% SCSA [96] and High Sn Bronze-route (B), 11% SCSA [97]), Nb_3Al (jelly-roll strands, 32% SCSA) [116], $(NbTa)_3Sn$ (11% SCSA) [117], $PbMo_6S_8$ [134], MgB_2 (AIMI 18 Filament (39% Filament CS)) [94], $FeSe_{0.5}Te_{0.5}$ (thin film IBAD substrates) [95] and $Ba(FeCo)_2As_2$ (thin film on CaF_2 substrates) [91] are also included. Closed and open symbols are used for anisotropic materials and signify that the magnetic field is parallel and perpendicular to the *ab*-plane respectively. Middle panel: J_c normalised by the superconducting depairing current density J_c/J_{DSc} (0 T, 4.2 K) as a function of normalised field B_{app}/B_{c2} (4.2 K) for the same materials as the upper panel. Values of J_{DSc} (0 T, 4.2 K) were calculated using the method outlined in the appendix. In anisotropic materials, the J_{DSc} (0 T, 4.2 K) associated with the direction of current flow (i.e. J_{DSc}^{ab} (0 T, 4.2 K)) were used. Lower panel: J_c normalised by its value at the $0.2B_{c2}$ (4.2 K) as a function of normalised field B_{app}/B_{c2}(4.2 K) for the same materials as the upper panels. The solid red curve was fitted using equation (2), with $p = 0.81$ and $q = 2.4$, and the dashed black curve was fitted using equation (3) with $\alpha = 2.8$ and $\beta = 0.29B_{c2}$(4.2 K). The fitting parameters were obtained without considering MgB_2.

Table 1. The depairing current density at zero magnetic field and 4.2 K, J_{DSc} (0 T, 4.2 K), and the parameters used to calculate it for important high-field superconductors. T_c is the critical temperature, ν is the exponent derived from the empirical equation $B_{c2}^c(T) = B_{c2}^c(0)(1 - (T/T_c)^\nu)$. The upper and lower critical fields B_{c1} and B_{c2} are given at 0 K and given for the magnetic field applied parallel to the *ab*-plane and parallel to the *c*-axis. For anisotropic materials, the G–L coherence length and G–L penetration depth are given parallel to the *ab*-plane, the *c*-axis as well as an angular average at 0 K. Anisotropic material parameters are taken from single crystals. Parameters for high-field isotropic superconductors were taken from wires. Parameters that were obtained from temperature-dependent experiments in the literature have the relevant reference cited next to them. Calculated parameters are labelled with an uppercase star: *. For Nb[†]: critical values are at 5 K and B_{c2} were estimated from extrapolating critical current data to zero [12]. For (NbTa)₃Sn[†]: B_{c1} was taken to be the same as Nb₃Sn. For Bi₂Sr₂Ca₂Cu₃O₁₀[†]: ν was taken to be the same as Bi₂Sr₂CaCu₂O₈; The value of ν is small, determined from high temperature data.

Material	T_c (K)	ν		$B_{c2}(0)$ (T)	$B_{c1}(0)$ (mT)	$\xi(0)$ (nm)	$\lambda(0)$ (nm)	$J_{DSc}(0, 4.2)$ (10^{12} Am^{-2})
Nb (5 K)	7.50 [12]	1.4 [114]		2.61[†]	34.3*	9.67*	79.0[†] [14]	0.322*
NbTi	8.99 [15]	1.8 [15]		15.7 [15]	13.5*	3.40*	163 [14]	0.434*
PbMo₆S₈	13.7 [115]	1.7 [115]		56.0 [115]	6.40 [115]	1.89*	265*	0.441*
Nb₃Al	15.6 [116]	1.3 [116]		26.5 [116]	68.7*	3.15*	65.0 [52]	4.74*
(NbTa)₃Sn	16.8 [117]	1.1 [117]		32.0 [117]	38.0[†]	3.06*	91.9*	2.53*
Nb₃Sn	17.8 [118]	1.5 [31]		29.5 [118]	38.0 [119]	2.73*	93.5*	2.83*
MgB₂	38.6 [120]	*ab*:	0.75 [120]	25.5 [120]	38.4 [120]	7.07*	97.1*	1.27*
		c:	0.72 [120]	9.20 [120]	27.2 [120]	2.44*	282*	0.439*
		$\langle\,\rangle$:				3.74*	129*	0.980*
Ba(FeCo)₂As₂	25.8 [121]	*ab*:	1.8 [121]	64.7 [121]	4.76*	2.18*	350 [122]	0.289*
		c:	1.2 [121]	56.4 [121]	3.75*	1.26*	605*	0.167*
		$\langle\,\rangle$:				1.86*	413*	0.246*
FeSe₀.₅Te₀.₅	14.0 [123]	*ab*:	3.0 [123]	44.0 [123]	2.00 [124]	2.16*	317*	0.272*
		c:	1.5 [123]	47.0 [123]	4.50 [124]	1.15*	593*	0.145*
		$\langle\,\rangle$:				1.80*	381*	0.228*
YBa₂Cu₃O₇₋ₓ	90.0 [20]	*ab*:	2.7 [20]	250 [20]	9.15*	1.29*	135 [19]	4.00*
		c:	1.7 [20]	120 [20]	23.3*	0.378*	894 [19]	0.604*
		$\langle\,\rangle$:				0.969*	208*	2.65*
Bi₂Sr₂CaCu₂O₈	84.8 [125]	*ab*:				3.24*	300 [125]	0.321*
		c:	0.14 [26]	231 [26]	4.60*			
		$\langle\,\rangle$:						
Bi₂Sr₂Ca₂Cu₃O₁₀	108 [23]	*ab*:				2.86*	165 [126]	1.22*
		c:	0.14[†]	297 [23]	13.8*			
		$\langle\,\rangle$:						

to one or other field dependence does not provide evidence for, or distinguish between, which mechanism operates [31].

It is long-known that wide, insulating grain boundaries prevent supercurrent crossing them. In this paper, we provide a quantitative description of when grain boundaries can be considered sufficiently resistive to limit J_c using our data on both microcrystalline and nanocrystalline YBCO. We have chosen these materials because: their fundamental properties in single crystal form are well known; the polycrystalline materials presented here provide a huge range of super-conducting transport properties; and there is a huge com-mercial potential if cheap polycrystalline HTS materials can be fabricated with high J_c. In addition, our group has devel-oped the expertise to make good nanocrystalline materials [32–37]. The approach we have adopted is to try to make a sufficiently broad range of YBCO samples and measurements to enable us to identify whether J_D or J_P limits J_c. The

structure of this paper is as follows: section 2 of this paper describes the sample fabrication process and the microstructure of the materials studied. The results from the transport and magnetic measurements used to characterise the samples are shown in section 3. Section 4 provides the theoretical con-siderations we have used to analyse our data and that of the literature. In section 5, we discuss our YBCO data and consider other high-field superconductors, in particular Nb₃Sn. Finally, the conclusions are summarised in section 6.

2. Fabrication of nanocrystalline materials

2.1. Sample milling and HIP'ing

Samples with two different compositions were made for this work —Y1: YBa₂Cu₃O₇₋ₓ and Y2: 75 wt% YBa₂Cu₃O₇₋ₓ + 25 wt%

Table 2. The fabrication process, transport and magnetic properties of the microcrystalline and nanocrystalline samples in this paper. 'Y1' and 'Y2' represent Y123 and Y123 + Y211 + CeO_2 compositions respectively. The letters 'P', 'M', 'H', and 'A' stand for pressed powders, milled, HIP'ed and annealed respectively. Milled samples (M) were milled for 30 h. HIP processing (H) was at 400 °C and 2000 atm for 5 h. Letter 'A' denotes the standard annealing heat treatment used, which includes a dwell at 750 °C for 20 h followed by 450 °C for 60 h. Ramping between temperatures was completed at 600 °C h^{-1}. A* denotes using heat treatment A, but with a ramp rate of 60 °C h^{-1}. B denotes a dwell at 450 °C for 20 h, followed by heat treatment A. A × 2 and A × 3 were heat treated using heat treatment A, twice and three times respectively. T_c was determined from the onset of ACMS data. 'Para' indicates a sample behaves paramagnetically and that no T_c was measured. $B_{Irr}(0)$ was determined by extrapolation from variable temperature susceptibility data (figure 13) and equation (8). $\mu_0 \Delta M / \Delta B$ is from d.c. magnetisation hysteresis measurements. $J_c^m(0, 4.2)$ is the magnetisation critical current density at zero field and 4.2 K unless otherwise stated, calculated using the grain dimensions of the samples. J_c^t is the transport critical current density at a 1 mV m^{-1} criterion. ρ_N (300 K) is the normal state resistivity at 300 K. The symbol '—' denotes that the property was not measured.
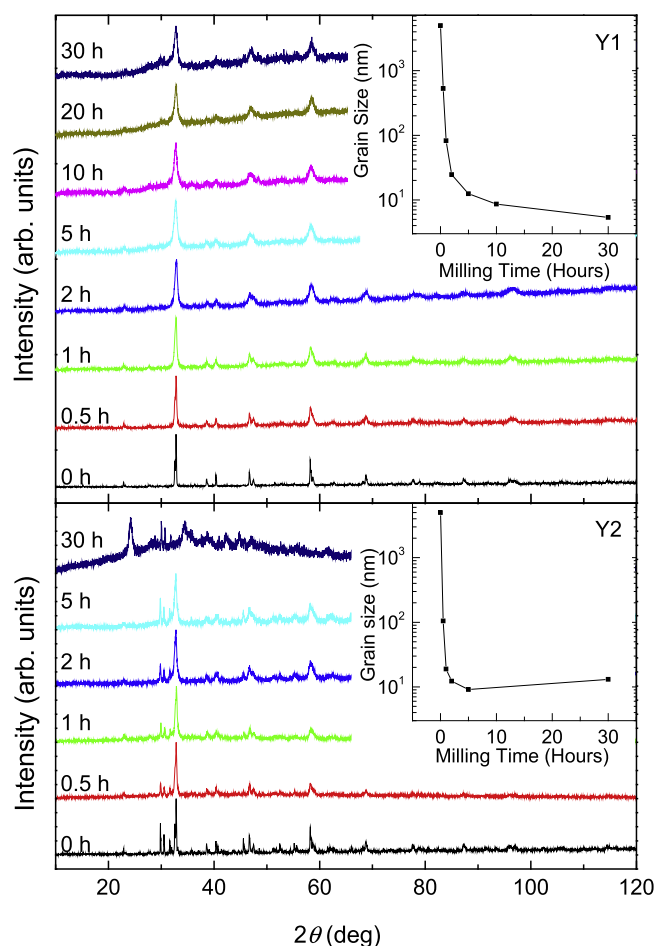
Sample	Grain size (nm)	Annealed	T_c (K)	$B_{Irr}(0)$ (T)	$\dfrac{\mu_0 \Delta M}{\Delta B}$	$J_c^m(0, 4.2)$ (A m^{-2})	J_c^t (A m^{-2})	$\rho_N(300\ K)$ (Ω m)
Y1P	5000	—	81	140	-2×10^{-1}	8.3×10^{10}	—	—
Y1H	5000	—	53	70	-3×10^{-2}	4.1×10^{10}	—	—
Y1HA	5000	A	86	163	-2×10^{-1}	2.9×10^{11}	1.2×10^5 (0.1 T, 4.2 K)	7.1×10^{-5}
Y1MH	20	—	Para	—	—	—	—	62
Y1MHA(1)	100	A	Para	—	-4×10^{-4}	9.3×10^9	Resistive	2.5×10^{-2}
Y1MHA(2)	100	A*	Para	—	-6×10^{-4}	1.0×10^{10} (10 K)	Resistive	2.0×10^{-2}
Y1MHA(3)	100	B	70	66	-3×10^{-3}	4.5×10^{10}	Resistive	8.9×10^{-3}
Y1MPA	25	A	73	40	-2×10^{-3}	2.7×10^{10}	—	—
Y2P	5000	—	81	119	-1×10^{-1}	5.1×10^{10}	—	—
Y2H	5000	—	53	62	-2×10^{-2}	4.0×10^{10}	—	—
Y2HA	5000	A	83	132	-2×10^{-1}	1.5×10^{11}	—	—
Y2MHA(1)	100	A	Para	—	—	—	—	1.0×10^{-2}
Y2MHA(2)	100	A × 2	Para	—	-7×10^{-4}	1.7×10^{10} (10 K)	70 (0 T, 2 K)	5.2×10^{-3}
Y2MHA(3)	100	A × 3	17	—	—	—	—	—

Y_2BaCuO_5 to which an additional 1 wt% CeO_2 was added [38, 39]. Commercial $YBa_2Cu_3O_{7-x}$, Y_2BaCuO_5 (99.98%, Toshima) and CeO_2 powders (99.99%, Alfa Aesar) were used to fabricate the samples. The Y1 samples were produced from the commercial powders directly. The Y2 composition was chosen because of its high J_c in bulk single crystal form [40]. Powders were first mixed together by shaking the starting powders for 30 min in a stainless steel vial using a SPEX 8000D high-energy shaker mill. Next, samples were milled using the miller and tungsten carbide (WC 94/Co 6) milling media in an argon atmosphere. In an earlier pilot study, we used copper milling media [35]. Although it is expected that copper is less detrimental to the superconducting properties of YBCO than WC or Co, we choose not to use Cu milling media in this work because it is too soft. The samples were milled in batches of 10 g, with a ball-to-powder mass ratio of 3:1, for a total of 30 h. The milling vial and balls were scraped with a tungsten carbide rod regularly, in argon, to increase yield and improve homogeneity. The powders were placed into small niobium foil packets (0.025 mm thick, 99.8%, Alfa Aesar), which acted as a diffusion barrier and then consolidated using a hot isostatic press (HIP). The Nb packets were sealed into stainless steel tubes (type 316, 1 mm thickness) and HIP'ed at a temperature of 400 °C and pressure of 2000 atm for 5 h. Many samples were subsequently annealed in pure flowing oxygen atmosphere in a dedicated oxygen furnace to optimise oxygen content and restore some crystallinity. In this paper, the letters 'P', 'M', 'H' and 'A' denote that a sample has been processed through a combination of powder or pellet Pressing,

Milling, HIP'ing, or Annealing respectively. The letters are added after the label for composition in the order that they occurred during processing. Table 2 lists the microcrystalline and nanocrystalline samples where the superconducting properties have been studied in detail.

2.2. X-ray diffraction (XRD) and SEM

The phases present and grain sizes of the samples were obtained using powder XRD measurements. Figure 2 shows the evolution of the XRD spectra for the as-supplied powders with the compositions Y1 and Y2, after they were milled for up to 30 h. Both compositions show similar behaviour, namely the peaks broadened with increased milling time. The associated decrease in the grain size of the $YBa_2Cu_3O_{7-x}$ was calculated using TOPAS Academic software and Rietveld refinement. The insets show the grain size as a function of milling time. The grain size of the as-supplied materials is estimated to be 5 μm from SEM (not shown). Within the first 5 h of milling, the grain size is drastically reduced by 3 orders of magnitude down to the nanometre scale. After 30 h, the reduction in grain size saturates as it reaches <10 nm. Figure 3 shows the XRD spectra of the MP, MH and MHA samples. The additional peaks at 30° in the Y1MHA(1) 30 h milled sample and at 24° in the Y2MHA(1) 30 h milled sample should be interpreted with care. We attribute these peaks predominantly to our samples being ground in air for and prior to XRD measurement itself, and the known high sensitivity of $YBa_2Cu_3O_{7-x}$ to decomposition to parent
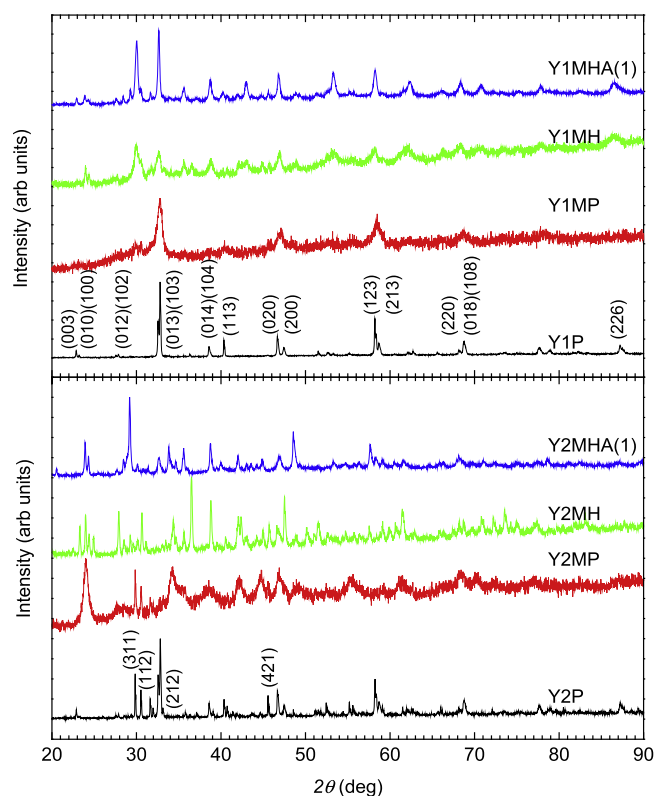
Figure 2. X-ray diffraction patterns for the composition Y1 (upper panel) and the composition Y2 (lower panel) after milling for up to 30 h. Inset: grain size as a function of milling time. The 5 μm data point in the as-supplied material (at 0 h) is obtained from scanning electron microscopy.

Figure 3. Upper panel: x-ray diffraction patterns for Y1P, Y1MP, Y1MH and Y1MHA(1). The main $YBa_2Cu_3O_{7-x}$ peaks are labelled. Lower panel: x-ray diffraction patterns for Y2P, Y2MP, Y2MH and Y2MHA(1). In addition to the $YBa_2Cu_3O_{7-x}$ peaks labelled in the upper panel, the main Y_2BaCuO_5 peaks are labelled in the lower panel.

oxides and Y_2BaCuO_5 in the presence of water vapour in air, particularly in highly milled samples [41–43]. We do not expect such decomposition to occur in our bulk HIP'ed samples that were not exposed to air. We have not identified the peak at 29° in the Y2MHA(1) sample. The grain size of the MHA samples is approximately 100 nm, with a relatively large uncertainty of a factor of 2, due to the unidentified peaks and high strain in these materials that complicates the refinement process. Trace amounts of WC were found in the XRD and EDX (not reported here) in some milled materials of both Y1 and Y2 compositions. There exist methods in which the oxygen content of $YBa_2Cu_3O_{7-x}$ can be calculated using an analysis of the *c*-axis lattice parameter, however we were unable to apply such analysis to our samples because of the very high strain content in these milled materials [44].

2.3. Thermal gravimetry (TG)/differential scanning calorimetry (DSC)

Figure 4 shows the TG and DSC data for the P, MP and MHA samples for both Y1 and Y2 compositions. Data were obtained over two cycles. In each cycle, samples were heated
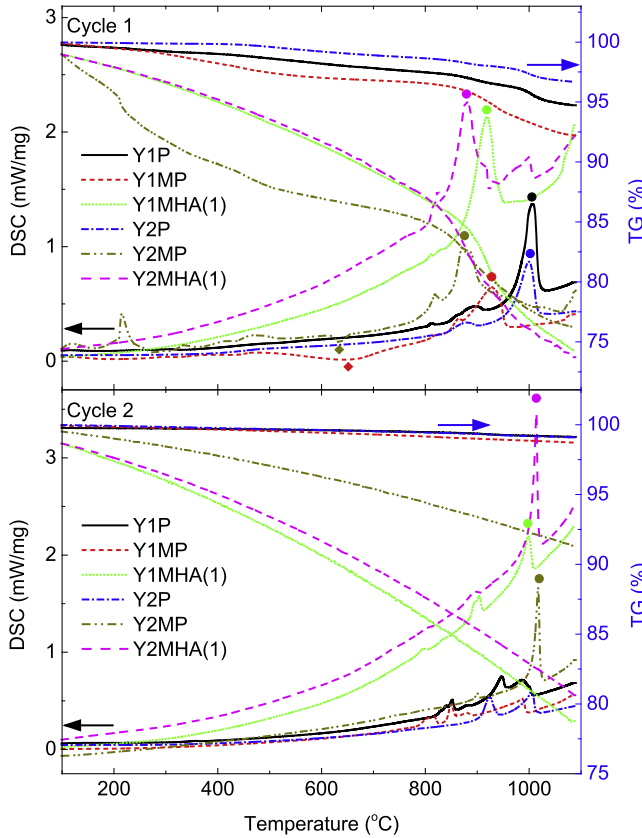
up to 1100 °C and cooled back to room temperature in a pure argon atmosphere at 10 °C min^{-1}. As was the case for the XRD data, one has to be careful interpreting the data for the highly milled samples. Although the DSC/TG samples were not powdered, they were exposed to air when they were transferred into the DSC/TG sample-holder cups prior to measurement. In particular, any significant mass loss or DSC peaks below 200 °C are usually associated with moisture.

Both TG and DSC data for the (as-supplied) Y1P and Y2P samples are in broad agreement with equivalent data from the literature [35]. The mass losses between 400 °C and 800 °C are consistent with oxygen loss of $YBa_2Cu_3O_{7-x}$ phase from O$_7$ to O$_6$ and there are large endothermic melting peaks with onsets at 970 °C [35]. The Y1P, Y1MP and Y2P samples were most stable to mass loss during both cycles. The other three samples showed mass loss over the entire temperature range during both cycles. The only clear exothermic peaks were observed at about 630 °C as indicated by the ♦ symbols for the Y1MP and Y2MP milled samples in the first cycle. We associate these peaks at ∼630 °C with crystallisation of amorphous, and recrystallisation of nanocrystalline phases, to produce larger grain sizes [45]. As expected, such peaks were not present in unmilled samples Y1P or Y2P nor in any of the second cycle data for any of the samples. These results led us to choose a HIP temperature of 400 °C to

Figure 4. Differential scanning calorimetric signal and thermogravimetric signal (showing percentage mass change) for Y1P, Y1MP, Y1MHA(1), Y2P, Y2MP, Y2MHA(1) samples between 100 °C and 1100 °C, at 10 °C min^{-1}. Upper panel: the heating part of the first cycle. Lower panel: the heating part of the second cycle. Significant endothermic peaks, associated with melting are labelled with ● symbols and exothermic peaks, associated with the crystallisation of amorphous and recrystallisation of nanocrystalline phases, by the ◆ symbol.

fabricate the YBCO materials in this work, to prevent excessive grain growth and follow an approach we have successfully used before to make other nanocrystalline materials [32–37]. In the two samples that were milled, HIP'ed, and annealed (Y1MHA (1) and Y2MHA(1)), there was increased and significant mass loss near 850 °C in cycle 1 and coincident large endothermic peaks, both of which are absent in cycle 2. We attribute these peaks to melting and oxygen loss. At the highest temperatures of the cycles, we associate the large endothermic melting peaks in figure 4 as follows: the peaks that occur in both panels near 1000 °C are due to melting of the YBa$_2$Cu$_3$O$_{7-x}$ phase—the exact melting temperature is dependent on oxygen content [46] and expected to be lower in argon atmosphere than in air [47]. The peaks with an onset near 993 °C are due to the reactions Y$_2$BaCuO$_5$ + BaCuO$_2$ → Liquid and YBa$_2$Cu$_3$O$_{7-x}$ + BaCuO$_2$ → Y$_2$BaCuO$_5$ + Liquid [48]. The peaks with an onset near 875 °C are due to the reaction YBa$_2$Cu$_3$O$_{7-x}$ + BaCuO$_2$ + CuO → Liquid [48]; and the peaks near 839 °C to melting of BaCuO$_2$ phase [35].
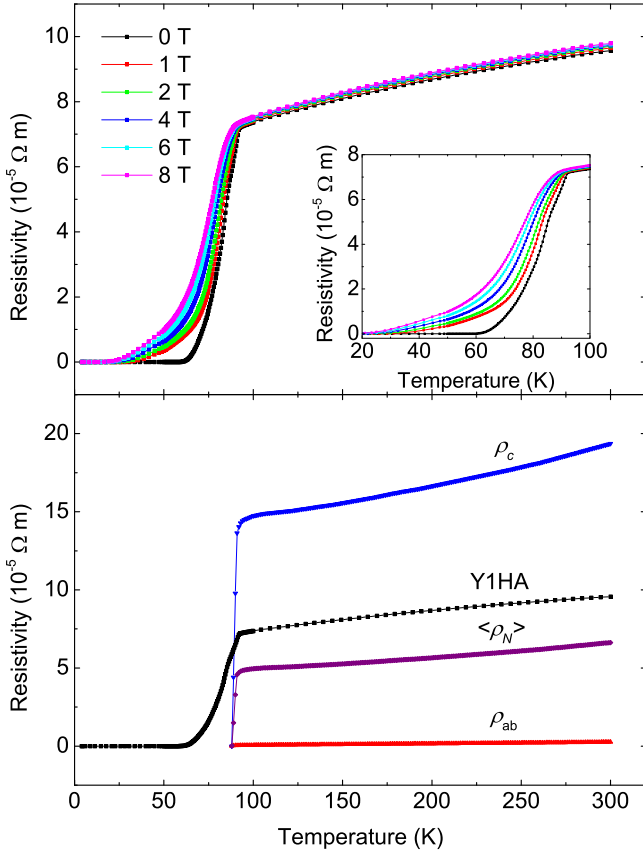

Figure 5. Resistivity as a function of temperature for all the materials of Y1-composition and the Y2MHA(1) and Y2MHA(2) samples. The strong effect of oxygen annealing can be seen in both micro and nanocrystalline materials, decreasing ρ_N(300 K) by a factor of $\sim 10^2$ and 10^3 respectively. However only three nanocrystalline materials showed a superconducting transition: Y1MHA(3), Y2MHA(1) and Y2MHA(2). Single crystal literature data were taken from [81].

3. Experimental results and analysis

3.1. Transport measurements—resistivity and critical current density

HIP'ed samples were shaped into cuboid bars for transport measurements with typical dimensions of $1 \times 1 \times 5$ mm. The samples were mounted onto a physical property measurement system (PPMS) resistivity puck [49]. Current and voltage leads were connected to the sample using silver paint for standard four-terminal measurements. The voltage taps were typically 2.5 mm apart. Control and measurement of the temperature and the magnetic field were made using the PPMS. To measure V–I traces, the puck was connected to external high-precision voltmeter and current sources. The current was supplied by a Keithley 220 programmable current source. A resistor was added in series to the sample in order to confirm that the current through the sample was equal to the nominal output current in the range of 10 nA–0.1 A. The voltage across the sample taps was measured with a Keithley 2100 6½ digit multimeter, with an additional ×50 000 amplifier [50] when required, to measure extremely small voltages. Figure 5 shows a summary of the resistivity data for the samples in this paper as a function of temperature, measured using excitation currents of typically 5 mA.

The YBCO microcrystalline sample that was simply HIP'ed (Y1H) has a weak temperature-dependent resistivity with no evidence of superconductivity. Oxygen annealing decreased ρ_N(100 K) by more than a factor of 10^3 and a superconducting transition was observed, which can be seen in the in-field data in the upper panel of figure 6 for sample Y1HA. In zero magnetic field, the onset T_c is 92 K and zero-resistivity occurs at 60 K. Figure 6 shows that as the applied field was increased, the onset T_c, that we associate with the grains, does not vary significantly, whereas the zero-resistivity

Figure 6. Upper panel: resistivity of Y1HA sample measured in fields of 0–8 T with a constant excitation current of 5 mA. Inset: detail of the two-step transition. Lower panel: resistivity of Y1HA in zero field compared to the resistivity of a single crystal of YBCO along the *c*-axis (ρ_c) and along the *ab*-planes (ρ_{ab}) [81] and the angular averaged resistivity $\langle \rho_N \rangle$ calculated using equation (16).

T_c, likely associated with the grain boundaries, is very significantly decreased. These findings are consistent with those of Dimos *et al* [51] where the largest suppression of superconductivity in relatively small fields occurs at the grain boundaries. 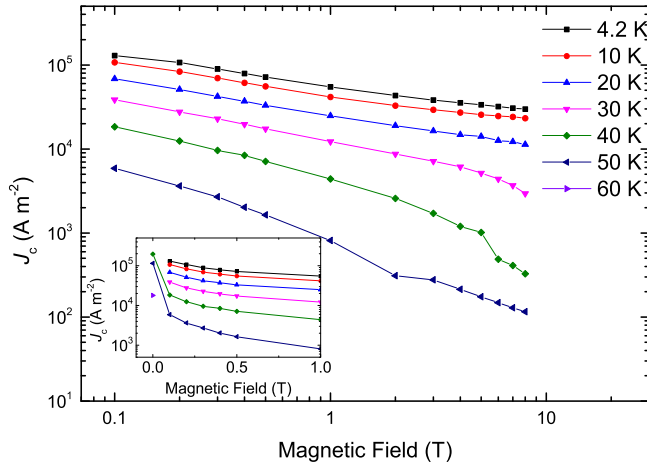The lower panel compares the values of ρ_N for Y1HA to those of single crystals in which current flows either along the *c*-axis direction or along the *ab*-plane. Figure 7 shows the equivalent *V–I* traces for Y1HA. The *V–I* traces show superconductivity between 0 and 8 T at 4.2 K. Zero field *V–I* data were also obtained up to 120 K in steps of 10 K, and thereafter up to 300 K in steps 50 K. Using a 1 mVm^{-1} criterion, the transport J_c is 1.2×10^5 Am^{-2} at 0.1 T and 4.2 K. Figure 8 shows the transport J_c of Y1HA determined using the same criterion. The inset includes the zero field J_c from 40 and 60 K. As shown later in section 3.3, the intragranular magnetisation J_c in this sample is of the order of 10^{11} Am^{-2}. Hence the transport J_c values measured here are six orders of magnitude lower than the intragranular currents.

As can be seen in figure 5, the nanocrystalline materials have resistivity values typically three or four orders of magnitude higher than microcrystalline materials. Y1MH sample has the highest ρ_N of all the samples—60 Ωm at 300 K. For comparison, the values of the resistivity of a good metal like Cu and a good insulator like diamond are 10^{-8} Ωm and

Figure 7. Upper: voltage as a function of current (*V–I*) of Y1HA sample at 4.2 K and various magnetic fields. The dashed lines show the electric field criteria of 1 mV m^{-1} and 100 μV m^{-1}. Lower: *V–I* data from 40 to 70 K at zero field.

10^{10}–10^{11} Ωm [52]. After annealing, the resistivity decreased by a factor of approximately 10^3 at room temperature. A smaller, further reduction was found by repeating the annealing process as in the case for Y2MHA(1) and Y2MHA (2). The *V–I* traces of nanocrystalline Y1MHA(1), (2) and (3) were entirely resistive with no signs of percolating supercurrents. Y1MHA(3) shows an inflection in ρ_N at 60 K which can also be seen in ac magnetisation discussed in section 3.2. We tried many different annealing procedures to produce supercurrents flowing across grain boundaries. A single nanocrystalline sample showed evidence that it could transport an intergranular supercurrent. Figure 9 shows the in-field resistivity of nanocrystalline materials of the Y2 composition. This sample was annealed twice. The data after the first annealing, Y2MHA(1), is given by solid symbols, and the data after the second annealing, Y2MHA(2), is given by the open symbols. The

Figure 8. Transport J_c of Y1HA as a function of field and temperature using $1\,mV\,m^{-1}$ criterion from 4.2 to 60 K. The inset shows the zero-field data obtained.

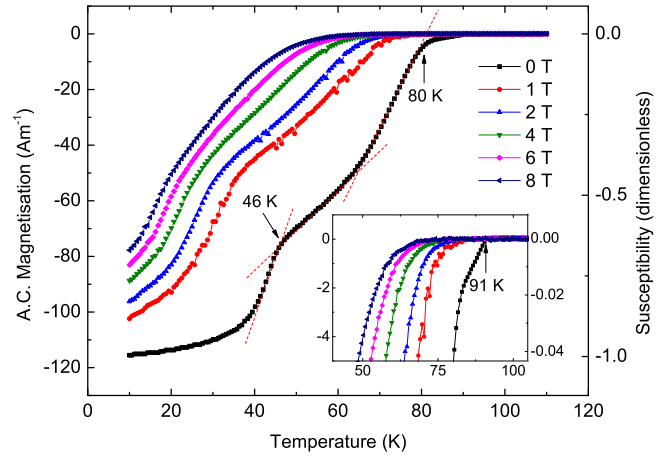**Figure 9.** The resistivity of the Y2MHA(1) sample (solid symbols) as a function of temperature in fields of up to 8 T (measured with an excitation current of 10 μA). At zero field, the peak resistivity is at 52 K and the resistivity does not reach zero at 2 K. The Y2MHA(2) data at zero field is the open squares. The resistivity has decreased at all temperatures and the temperature at which peak resistivity has increased to 64 K. Inset: voltage as a function of current of Y2MHA(2) at 2 K and 0 T, showing evidence for very weak superconductivity.
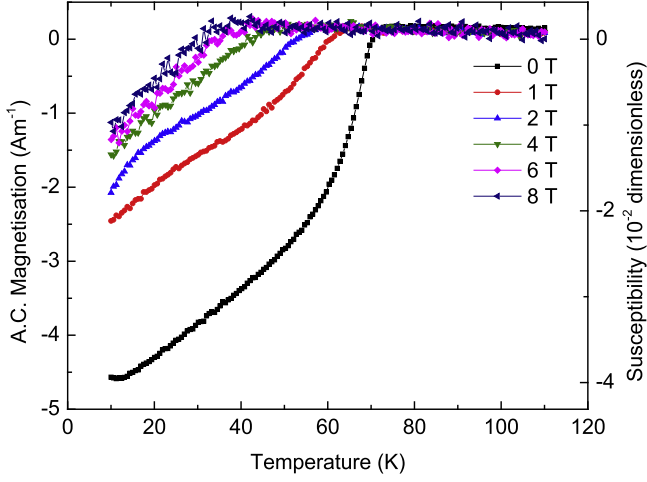

Figure 10. Ac magnetisation and magnetic susceptibility as a function of temperature of Y1P sample. The dimensions of the sample were $1 \times 1 \times 1$ mm. Inset: detail showing the small onset signal transition with $T_c = 91$ K at zero field. The data were taken with an excitation field of 0.4 mT at a frequency of 777 Hz.

second annealing decreased the resistivity by at least a factor of 2 over the entire temperature range. The inset shows the V–I trace of the sample after the second annealing, measured at 2 K and 0 T. It provides evidence for very weak superconductivity. The transport J_c at 2 K and 0 T was very small, equivalent to about $70\,Am^{-2}$ at an electric field criterion of $1\,mV\,m^{-1}$. This is at least 10^9 times lower than the transport J_c of commercial YBCO tapes.

3.2. AC magnetic susceptibility

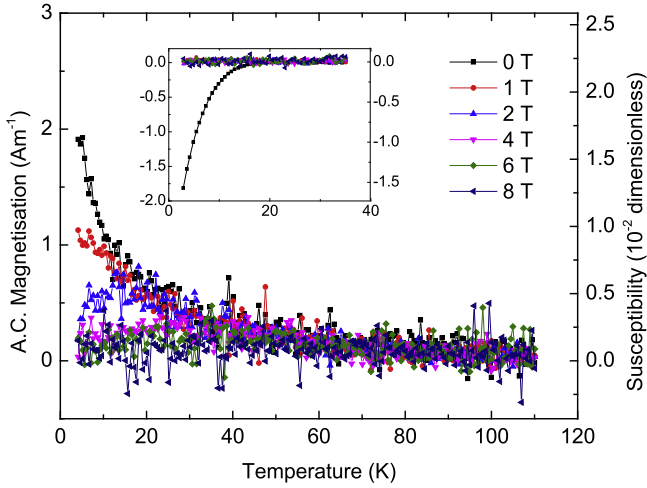The ac magnetic susceptibility and dc magnetisation measurements were all taken in our Quantum Design PPMS

system [53]. The non-HIP'ed samples were pressed into pellets with a typical size of 3 mm diameter and a height of 2 mm. The HIP'ed samples were shaped into cuboids with fine emery paper, with typical dimensions of $1 \times 1 \times 1$ mm. The ac magnetisation measurements were taken with an excitation field of 0.4 mT and 777 Hz (equivalent to $0.3\,T\,s^{-1}$).

Figure 10 shows the ac magnetisation (and equivalent susceptibility) of the microcrystalline Y1P material with very broad transitions to the superconducting state. The inset shows the onset signal at 91 K, which shows an inflection at ∼80 K. There is a large signal with a second transition centred at ∼46 K. This granular sample is a pressed powder in which one can expect that the electronic powder–powder connections to be weak. We attribute the high temperature transition to the individual grains becoming superconducting and producing a large screening signal. The low temperature transition at 46 K is attributed to stronger coupling across the grains, allowing sufficiently large intergranular currents (flowing on the scale of the sample size) at low temperatures, to produce an additional signal. The signal of $-115\,Am^{-1}$ from this sample characterises full screening for our experimental conditions at the lowest temperature and is used to normalise susceptibility values to negative unity.

However, for most of our HIP'ed nanocrystalline samples, large paramagnetic backgrounds with no superconducting transitions were found in the susceptibility data. A small superconducting signal was recovered in the Y1MHA (3) sample after oxygen annealing, as shown in figure 11. This sample has a T_c of ∼70 K, but a low susceptibility of -4.0×10^{-2} at 4.2 K in zero field. Figure 12 shows typical data for nanocrystalline materials with Y2 composition, which show temperature-dependent paramagnetic-like behaviour. The Y2MHA(3) data in the inset did show a superconducting transition at ∼17 K in zero field with a susceptibility of -1.5×10^{-2} at 4.2 K, although no signals associated with superconductivity were observed in the

Figure 11. Ac magnetisation and magnetic susceptibility as a function of temperature of Y1MHA(3) sample. The data were taken with an excitation field of 0.4 mT and at a frequency of 777 Hz.
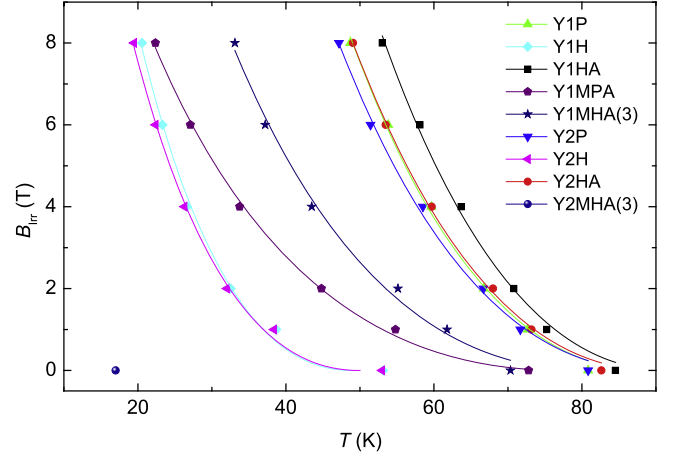

Figure 12. Ac magnetisation and magnetic susceptibility as a function of temperature of Y2MHA(2) sample. No superconductivity is observed. Inset: ac magnetic susceptibility as a function of temperature of Y2MHA(3) sample which was annealed three times. The data were taken with an excitation field of 0.4 mT and at a frequency of 777 Hz.

in-field data. Nevertheless, it is important to realise that while most nanocrystalline samples showed no superconducting ac screening signals (or more accurately, signals below our noise floor), they were in fact superconducting as demonstrated by the very sensitive dc magnetisation measurements shown in the next section. When screening currents are entirely within very small grains, the susceptibility is reduced by a factor χ'_g/χ'_b [54, 55] where

$$\frac{\chi'_g}{\chi'_b} = \frac{1}{15}\left(\frac{a^2}{\lambda^2}\right)f(a, \xi_{BCS}) \text{ for } \lambda > a, \tag{4}$$

where χ'_g and χ'_b are the granular and bulk (intergranular) susceptibilities respectively and a is the grain size. The factor $f(a, \xi_{BCS})$ accounts for non-local effects associated with the BCS coherence length (ξ_{BCS}). Low values of $f(a, \xi_{BCS})$ occur when the grain size is much smaller than ξ_{BCS} which is about

Figure 13. Irreversibility field as a function of temperature of all the micro and nanocrystalline fabricated samples. B_{Irr} is defined as the onset in susceptibility measurements and the data fitted using an equation of the form of equation (8).

4–7 nm [56] for YBCO. It has a value of unity when $a \gg \xi_{BCS}$. The nanocrystalline samples in this work have grain sizes of 100 nm (see table 2) so we assume $f(a, \xi_{BCS}) = 1$.

For an anisotropic superconductor, we can find an approximate value for the angular dependence of the G–L penetration depth ($\lambda(\theta)$) from the angular dependence of the G–L coherence length ($\xi(\theta)$) derived from upper critical field, and the angular dependence of the G–L constant ($\kappa(\theta)$) where $\lambda(\theta) = \kappa(\theta)\xi(\theta)$ [57] so that

$$\xi^2(\theta) = \xi_{ab}(\xi_{ab}^2\cos^2(\theta) + \xi_c^2\sin^2(\theta))^{\frac{1}{2}} \tag{5}$$

and

$$\lambda^2(\theta) = \lambda_{ab}^2\lambda_c/(\lambda_c^2\cos^2(\theta) + \lambda_{ab}^2\sin^2(\theta))^{\frac{1}{2}}. \tag{6}$$

By integrating equation (5) or (6) over all solid angles, we obtain an angular average where for example $\langle 1/\lambda^2(\theta)\rangle$, the angular average of the inverse of the G–L penetration depth squared, for a collection of random oriented grains, is

$$\left\langle\frac{1}{\lambda^2(\theta)}\right\rangle = \frac{1}{2}\int_0^\pi \frac{1}{\lambda^2(\theta)}\sin\theta d\theta. \tag{7}$$

Numerical integration of equation (7) with values of $\lambda_c = 916$ nm and $\lambda_{ab} = 138$ nm [19] and using an average grain size of 100 nm, gives $\langle\chi'_g/\chi'_b\rangle = 1.8 \times 10^{-2}$. This value is similar to that given in figure 11 for Y1MHA(3) and figure 12 inset for Y2MHA(3), consistent with a reversible ac signal entirely from within the nanocrystalline grains. We note that this calculation does not account for the induced moment and the applied field not being parallel or demagnetisation factors [58]. Figure 13 shows the irreversibility field ($B_{Irr}(T)$) as a function of temperature for our samples, taken from the onset of the ac susceptibility data. The data were fitted using the equation [31].

$$B_{Irr}(T) = B_{Irr}(0)(1 - t^{0.5})^{2.1}, \tag{8}$$

where $t = T/T_c$. The grains in the Y1HA and Y2HA samples have the highest superconducting critical properties of our

Figure 14. Magnetisation as a function of field for Y1P at temperatures from 4 to 90 K and between −2 and 8 T. The data at −2 T have a gradient of $\mu_0 \Delta M / \Delta B = -0.2$.

Figure 15. Critical current density as a function of field for Y1P, at temperatures from 4 to 90 K and between −2 and 8 T. Grain dimensions were used to calculate magnetisation J_c.

samples. Of the microcrystalline materials, Y1H and Y2H have among the lowest T_c and $B_{Irr}(0)$, lower than Y1MHA(3) and Y1MPA, which demonstrates the severity of the oxygen loss that the samples suffered during the HIP process. The onset T_c and $B_{Irr}(0)$ values derived using equation (8) are listed in table 2.

3.3. DC magnetic hysteresis

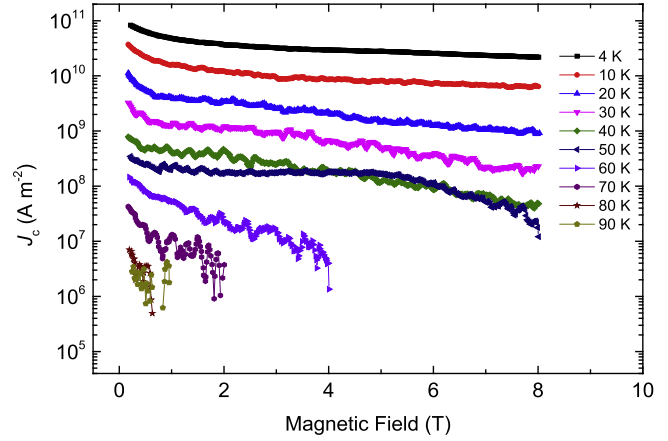Dc magnetisation hysteresis data were also taken with the PPMS. At each temperature, the field was swept from 0 T down to −1.5 T (or −2 T in some cases), then swept up to 8.5 T and back to −1.5 T. This approach meant we could extract values of $\mu_0 \Delta M / \Delta B$ as the magnetisation changed from the upper branch to the lower branch, as well as magnetisation J_c values calculated using Bean's model [59], as shown in table 2. For pellets of radius R and volume V,

$$J_c = 3 \frac{\Delta m}{RV}, \tag{9}$$

where Δm is the difference in magnetic moment between the increasing and decreasing field branches. For rectangular bars with length w and width b,
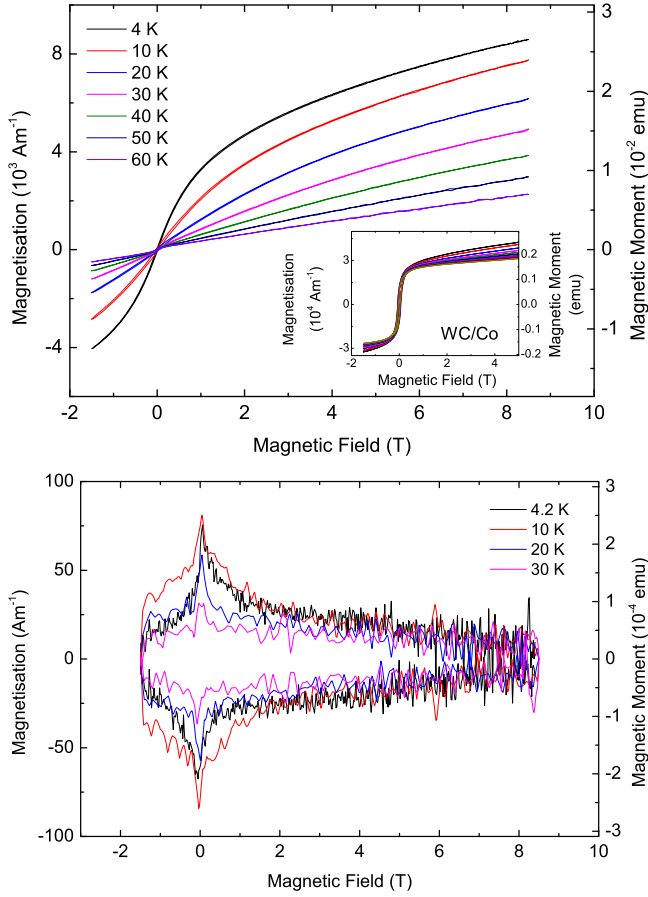
$$J_c = \frac{2\Delta m}{w\left(1 - \frac{w}{3b}\right)V}. \tag{10}$$

Typical hysteresis and J_c data for microcrystalline materials are shown in figures 14 and 15. In this paper, we assume that the currents flowing are either entirely intergranular or intragranular, or both. We set aside the possibility of clusters of well-connected grains. Given that the measured transport J_c is only of the order of 10^5 Am^{-2} in microcrystalline materials, intergranular J_c contributes typically less than 1% of the total dc magnetisation signal in-field and can be ignored. Hence we conclude that the dc magnetisation signal comes predominantly from hysteretic screening currents flowing within grains. The typical response for nanocrystalline materials is shown in figure 16. The data show a paramagnetic background with superconducting hysteresis
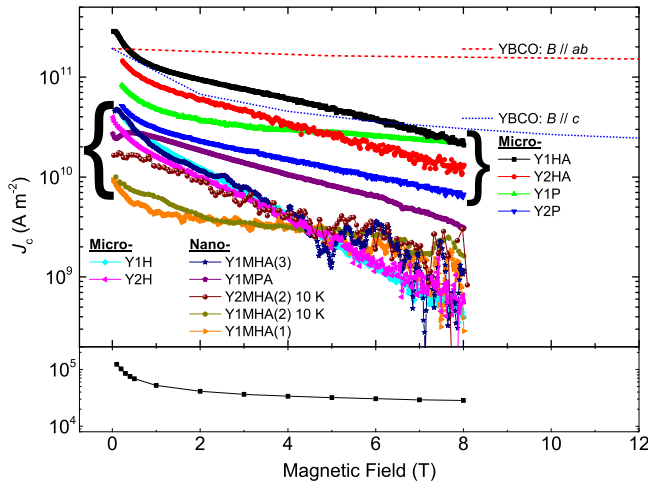
which has been observed in ac susceptibility data in other granular materials in the literature [60, 61]. The lower panel of figure 16 shows the data after the paramagnetic background has been subtracted, showing a typical Type-II superconductor hysteresis curve. Straumal *et al* [62, 63] have shown that in ZnO, a high density of grain boundaries leads to ferromagnetism even without doping, but also that the solubility of magnetic contaminants such as Co can significantly increase with the density of grain boundaries. To investigate the effect of contamination, the WC/Co vial and balls were milled without any powder (except for that caked onto the surfaces) which yielded mainly WC/Co powder with small amounts of YBCO. The contaminants were pressed into a pellet and measured using the same method as the superconducting samples. These data are shown in the inset of figure 16. The magnetisation of contaminants are temperature-independent around 0 T, which is different to the background from the sample, consistent with the expectation that the extent of WC/Co contamination and its ferromagnetic contribution to the magnetisation are low. Hence, as with the microcrystalline samples, the dc magnetisation signal from the nanocrystalline samples is almost entirely due to screening currents flowing within the grains. Figure 17 shows a compilation of the intragranular magnetisation J_c for both the microcrystalline and nanocrystalline samples (we note that the uncertainty in the grain size is typically about a factor of two) and also contains transport J_c values for commercial YBCO tape [13]. Given that in our polycrystalline samples the current flows both along the *ab*-planes and along the *c*-direction, whereas J_c values in commercial tapes only flows along the *ab*-plane for the two configurations given, figure 17 shows that the intragranular J_c values in our polycrystalline samples are high. The best microcrystalline samples have intragranular J_c comparable to that of tapes, and strikingly the field dependence for all the samples that have been annealed is very similar to the commercial tapes. The samples that were HIP'ed-only (Y1H and Y2H) show a more drastic decrease in J_c with magnetic field compared to other microcrystalline

Figure 16. Upper panel: hysteretic magnetisation of Y1MHA(1) sample. Inset: magnetisation of the milling materials (that are potential contaminants in the samples). Lower panel: the same hysteretic magnetisation data as the upper panel, after subtracting the paramagnetic background, that show typical Type-II hysteresis and temperature dependence.

Figure 17. Magnetisation J_c as a function of field for fabricated samples at 4.2 K (unless otherwise labelled). Grain dimensions were used to calculate magnetisation J_c. Transport J_c of Y1HA sample (shown in the lower panel) and YBCO commercial tape data are also included for comparison [13]. The best microcrystalline samples have intragranular J_c comparable to that of tapes.

Figure 18. Magnetisation hysteresis as a function of magnetic field in order to study field reversal for the Y1P sample at 4.2 K. Starting from zero field, the field was repeatedly ramped +1 T then −0.5 T, up to 8.5 T. Inset: field reversal data set showing the full range. The arrows show the direction of the hysteresis and have a gradient for $\mu_0 \Delta M / \Delta B = -0.2$.

samples, and at 8 T, have J_c comparable to that of the nanocrystalline group. We attribute the poorer in-field properties of some of our samples to the decrease in oxygen content during HIP'ing, consistent with the decrease in T_c and $B_{Irr}(0)$ seen in the ac susceptibility data. After annealing (Y1HA and Y2HA), T_c, $B_{Irr}(0)$ and J_c have all recovered. Compared to commercial YBCO tape, transport J_c of microcrystalline materials is 10^6 lower, and for nanocrystalline material Y2MHA(2) (not included on this graph) this difference increases to 10^9.

In addition to finding a clear intragranular signal associated with superconductivity for the nanocrystalline materials, not found using standard ac susceptibility measurements, we can use field reversal in the dc magnetisation measurements ($\mu_0 \Delta M / \Delta B$). With these data we can address the type of pinning. Using Bean's relation for a cylinder, $|\Delta B| = 2\mu_0 J_c R$ where $|\Delta B|$ is the magnitude of the field required to reverse the magnetisation, equation (9) gives [64]

$$\frac{\mu_0 \Delta M}{\Delta B} = -\frac{\frac{1}{3} J_c R}{2 J_c R} = -0.17, \quad (11)$$

where the negative sign comes from Lenz's law. Figure 18 shows minor hysteresis loops taken at 10 K for Y1P. The inset of figure 18 shows that $\mu_0 \Delta M / \Delta B$ is only weakly field dependent. At very low fields, $\mu_0 \Delta M / \Delta B$ increases, associated with the increased role of reversible screening currents flowing at the surface of the sample. The $\mu_0 \Delta M / \Delta B$ values in table 2 were obtained from the field reversal data at −1.5 or −2 T, calculated from the linear region during the initial field reversal. In most microcrystalline materials, typical values of $\mu_0 \Delta M / \Delta B$ are approximately −0.17, consistent with bulk pinning in Bean's model. For nanocrystalline materials, the values of $\mu_0 \Delta M / \Delta B$, derived from data similar to that in figure 16 are typically 3 orders of magnitude smaller. These small values, compiled in table 2, have been found in the work of Shimizu and Ito [65] and cannot be explained by bulk pinning using Bean's model. We attribute the low values to the

surface pinning in the grains, consistent with dc magnetisation signals that are predominantly intragranular. Hence, the magnetisation J_c we have calculated using grain size dimensions, provides a lower bound for the grain's surface pinning J_c.

4. Theoretical considerations

By using a combination of transport and ac magnetic susceptibility data, we can separately determine the magnitude of the intergranular current density and the intragranular current density. In this section we consider grain and grain boundary properties. We use our resistivity data and the theoretical considerations to explain why the transport current density is so low in our YBCO samples.

4.1. The limiting size for superconductivity

While fabricating nanocrystalline materials, it is reasonable to ask first, how small grains can be before they can no longer be considered bulk material. Deutscher *et al* [66] have provided three methods for calculating the minimum size required to sustain superconductivity in LTSs. The first is the condition that superconductivity is quenched when the fluctuations in the order parameter ($\delta\Psi$) are of the same order as the order parameter (Ψ_0), which leads to

$$\frac{\langle |\delta\Psi|^2\rangle}{|\Psi_0|^2} \approx \frac{k_B T}{2E_c V_{\min}}, \qquad (12)$$

where E_c is the condensation energy and $V_{\min}$ is the minimum volume of a grain that still sustains superconductivity. The second is when there is only one Cooper pair per grain so that

$$N(0)\Delta V_{\min} \approx 1, \qquad (13)$$

where $N(0)$ is the density of states at $T = 0$ and Δ is the superconducting energy gap. The third is when the separation of quasi-particle energy levels δ is of the order of Δ, which leads to the equation

$$r_{\min} = \left(\frac{8\pi}{3 \times 0.18}\xi_0 \lambda_F^2\right)^{\frac{1}{3}}, \qquad (14)$$

where $r_{\min}$ is the minimum radius and λ_F is the Fermi wavelength. Deutscher made assumptions that are only strictly justified for LTSs. However, if we naively apply these methods to YBCO, then we obtain $r_{\min} = 0.3$–1 nm (using literature values of $E_c = 0.063\ k_B T_c$ per unit cell [67], $N(0) = 2.10 \times 10^{28}\ \mathrm{m}^{-3}\,\mathrm{eV}^{-1}$ [68], $\Delta = 30\ \mathrm{meV}$ [59], $\lambda_F = 0.3$ nm [69] and $\xi_0 = 1.5$ nm [70]). These calculations suggest even the (100 nm) grains in our nanocrystalline YBCO are sufficiently large to be well within the bulk material regime.

4.2. The resistivity of the grain boundaries

Without understanding why high angle grain boundaries do not support high J_c, we cannot know why J_c is low in polycrystalline materials. The standard explanation for the Dimos results that showed J_c decreases with increased misorientation angle in [001] tilt boundaries is that grain boundaries act as 'weak-links'. However, this does not clarify whether the low J_c values found by Dimos were due to poor coupling across

the grain boundaries or weak flux pinning in the grain boundaries. TDGL calculations suggest that the surface properties at the ends of any junction strongly affect the current the junction can carry as well as the interior of the junction, which undermines comparisons between single junctions and bulk properties. Other possible explanations for low J_c values could include the nature of the fundamental mechanism for superconductivity itself or perhaps the underlying symmetry of the *d*-wave order parameter. The low carrier density or specific electronic structure that leads to HTS or the phononic structure may also have been responsible. Despite the range of possibilities, a review of the literature shows that in S-N-S junctions, the effective resistivity of the normal layer in the junction can easily vary from a factor of 10^2 times higher than the bulk resistivity of normal material in the junction, as found for Pb/Cd/Pb [71], and up to a factor of 10^4 times higher, as is the case for Nb/Al/Nb [72] [73], Pb/Cu/Pb [74] [75], and YBCO/Au/YBCO [76]. Recent work in our group on YBCO tapes has shown that large interfacial resistances of $2.5 \times 10^{-8}\ \Omega\,\mathrm{cm}^2$ can even occur between a silver interface and a YBCO layer [77]. Given the potential for highly resistive interfaces and highly resistive grain boundaries in YBCO, in this paper we try to quantify how much the high resistivity of the grain boundaries lowers the critical current density of polycrystalline YBCO. We consider the most simple case, where the grain boundaries are modelled as a highly resistive N-component (i.e. where the normal layer has $T_c = 0$) of an S-N-S junction.

We first calculate the expected resistivity of a randomly aligned polycrystalline YBCO sample with completely transparent grain boundaries (i.e. normal grain boundaries with zero resistivity). The angular resistivity $\rho_N(\theta)$ of a YBCO single crystal when the transport current is at angle θ with the *c*-axis in spherical coordinates is given by [78]:

$$\rho_N(\theta) = \rho_c \cos^2\theta + \rho_{ab}\sin^2\theta, \qquad (15)$$

where ρ_c is the resistivity along the *c*-axis and ρ_{ab} is the resistivity along the *ab*-plane. Integrating $\rho_N(\theta)$ through all solid angles, gives the angular averaged resistivity ρ_N where:

$$\langle\rho_N\rangle = \frac{1}{2}\int_0^\pi \rho_N(\theta)\sin\theta\,\mathrm{d}\theta = \frac{1}{3}(2\rho_{ab} + \rho_c). \qquad (16)$$

In equating $\langle\rho_N\rangle$ to the resistivity of a randomly aligned polycrystalline material, one is assuming that there is no redistribution or preferential percolation of the current along low resistivity paths. We can assess whether this approach is valid by considering polycrystalline graphite. Graphite is a good choice because it has very low resistivity grain boundaries. Single crystal resistivity values for graphite are: $\rho_{ab} = 6 \times 10^{-5}\ \Omega\mathrm{m}$ and $\rho_c = 6 \times 10^{-3}\ \Omega\mathrm{m}$ [79]. Polycrystalline graphite has a resistivity of $2 \times 10^{-3}\ \Omega\mathrm{m}$ [80] which is consistent with the value of $\langle\rho_N\rangle$ from equation (16). A similar calculation for YBCO using the resistivity of single crystals, where $\rho_{ab} = 6 \times 10^{-7}\ \Omega\mathrm{m}$ and $\rho_c = 1.5 \times 10^{-4}\ \Omega\mathrm{m}$ at 100 K [81], gives $\langle\rho_N\rangle = 5.0 \times 10^{-5}\ \Omega\mathrm{m}$. Figure 6 shows the resistivity of sample Y1HA and compares it to values for single crystals and $\langle\rho_N\rangle$. Sample Y1HA has a resistivity about 50% higher than $\langle\rho_N\rangle$. Given the very high values of critical

parameters for the grains of this material (T_c, $B_{Irr}(0)$ and magnetisation J_c^m), we attribute the enhanced resistivity (2.4×10^{-5} Ωm) to the resistivity of grain boundaries. Using a grain size of approximately 5 μm and a grain boundary thickness of approximately 1 nm [82] leads to a large grain boundary resistivity of $\rho_{GB} \approx 0.12$ Ωm. Using a similar approach to the resistivity data for the nanocrystalline materials in table 2, a grain size of 100 nm gives a very large grain boundary resistivity of $\rho_{GB} = 8.2$ Ωm. In terms of contact (areal) resistivity, the micro and nanocrystalline grain boundary resistivities are 1.2×10^{-10} Ωm^2 and 8.2×10^{-9} Ωm^2 respectively. These values can be compared to the contact resistivities for some [001] tilt grain boundaries in thin-film oxide bicrystals (including YBCO) [83], which are generally lower and in the range of 10^{-14}–10^{-11} Ωm^2. We note that one can expect the resistivity of grain boundaries with misorientation angles that can include all possible angles to be higher than the [001] tilt, strain-free bicrystal grain boundaries. The resistivity data in figure 6 for Y1HA also provide supporting evidence for the additional resistance of the grain boundaries being similar to that of the grains: after the initial onset of the superconducting transition of the grains at 92 K, there is an inflection at ∼83 K, which we attribute to the grain boundaries starting to carry significant current. The lower temperature part of the transition is much more strongly depressed by the magnetic field than the onset transition which is similar to that observed elsewhere [36] and consistent with the in-field properties of grain boundaries [3].

4.3. Depairing current density of the grain boundaries

In this section we calculate the reduction in the local depairing current density (J_{DN}) in the boundary caused by its high resistivity. Recently we have found analytic solutions to the G–L equations in zero field for the $J_{DN}(T)$ in a 1D S-N-S junction in the clean and dirty limit [8] where:

$$J_{DN}(T) \approx J_{DSc}(T) \sqrt{2} \frac{\rho_S \xi_S}{\rho_N \xi_N} \left\{ \sqrt{\left(\frac{\xi_S \rho_S}{\xi_N \rho_N \sqrt{2}}\right)^2 + 1} \right.$$
$$\left. - \frac{\xi_S \rho_S}{\xi_N \rho_N \sqrt{2}} \right\}^2 \exp\left(\frac{-2d}{\xi_N}\right), \quad (17)$$

where $J_{DSc}(T)$ is the depairing current density in the superconducting grain, ρ_S/ρ_N is the ratio of the resistivity in the grain to the grain boundary, ξ_S/ξ_N is the ratio of the G–L coherence length in the superconductor to the decay length of the order parameter in the normal grain boundary, and d is the thickness of the grain boundary. Because equation (17) provides zero-field values, we use it to provide upper bound values for J_{DN} in the grain boundaries of polycrystalline YBCO (ξ_S values in table 1 were used in these calculations). To simplify the analysis for the anisotropic materials, we have only considered angular averaged properties to calculate an angular average for J_{DN} (i.e. J_{DN} in table 3, where we have used

$$\langle J_{DSc}(T) \rangle \approx \frac{\Phi_0}{3\sqrt{3}\,\pi\mu_0} \left\langle \frac{1}{\lambda^2(T)\xi(T)} \right\rangle, \quad (18)$$

where $\langle\lambda\rangle$ and $\langle\xi\rangle$ are the angular average G–L penetration depth and G–L coherence length and can be found in table 1. The superconducting parameters in equation (17) are well established. Microscopic theory gives the clean coherence length as

$$\xi_{SClean}(T) \approx \frac{\hbar v_F}{1.76\pi k_B T_{cS}^{\frac{1}{2}}(T_{cS} - T)^{\frac{1}{2}}} \quad (19)$$

and the dirty coherence length

$$\xi_{SDirty}(T) \approx \left(\frac{\pi\hbar D_S}{8 k_B (T_{cS} - T)}\right)^{\frac{1}{2}}, \quad (20)$$

where T_{cS} is the critical temperature of the superconducting layer. We can use the relation for the diffusivity given by:

$$D_S \approx \frac{\pi^2 k_B^2}{3 e^2 \rho_S \gamma} = \frac{v_F l}{3} = \frac{m v_F^2}{3 e^2 \rho_S n}, \quad (21)$$

where the equivalent forms in equation (21) have been derived using standard relations [84] for resistivity and the Sommerfeld constant (γ), and also for the angular averaged Fermi velocity (v_F) and mean free path (l) in terms of number of valence electrons per unit volume (n). Accurate values of these microscopic parameters are critical to the calculation of J_{DN}. To test the validity of these values listed in table 3, we used Pippard's approach to find a coherence length ($\xi_{SPippard}(0)$) from the clean and dirty values [8] using

$$\xi_{SPippard}(0) \approx \left(\frac{1}{\xi_{SClean}(0)} + \frac{1}{\xi_{SDirty}(0)}\right)^{-1}. \quad (22)$$

We suggest that the microscopic parameters are reasonable values since a comparison between $\xi_{SPippard}(0)$ and $\xi_{Bc2}(0)$ (see table 3), shows they are similar. We have used the Ginzburg–Landau relation (that is strictly only valid close to T_c) to define $\xi_{Bc2}(0)$ where

$$B_{c2}(0) \approx \frac{\Phi_0}{2\pi\xi_{Bc2}^2(0)}. \quad (23)$$

Within the context of the G–L theory, the temperature dependence of $\xi_N(T)$ is given by

$$\xi_N(T) \approx \xi_N(T_{cS})\left(\frac{T_{cS} - T_{cN}}{T - T_{cN}}\right)^{\frac{1}{2}}. \quad (24)$$

We have followed Pippard's approach and related $\xi_{NPippard}(T_{cS})$ to the microscopic clean and dirty limits [8] using

$$\xi_{NPippard}(T_{cS}) \approx \left(\frac{1}{\xi_{NClean}(T_{cS})} + \frac{1}{\xi_{NDirty}(T_{cS})}\right)^{-1}, \quad (25)$$

where

$$\xi_{NClean}(T_{cS}) \approx \frac{\hbar v_F}{1.76\pi k_B T_{cN}^{\frac{1}{2}}(T_{cS} - T_{cN})^{\frac{1}{2}}}, \quad (26)$$

$$\xi_{NDirty}(T_{cS}) \approx \left(\frac{\pi\hbar D_N}{8 k_B (T_{cS} - T_{cN})}\right)^{\frac{1}{2}}, \quad (27)$$

in which D_N is the normal layer equivalent of D_S as given by equation (21) and T_{cN} is the critical temperature of the normal

Table 3. Resistivity of the normal layer ρ_N at T_c, Sommerfeld constant (γ), Fermi velocity (v_F), the superconducting layer coherence length in the clean and dirty limits (ξ_{SClean} and ξ_{SDirty}), comparison of the Pippard coherence length $((\xi_{SPippard})^{-1} = (\xi_{SClean})^{-1} + (\xi_{SDirty})^{-1})$ with the $\xi_{B_{c2}}(0)$ coherence length calculated from B_{c2} where $(\xi_{B_{c2}}(0) = (\Phi_0/2\pi B_{c2}(0))^{\frac{1}{2}})$, the normal layer diffusivity (D_N) calculated using γ values, decay length of the normal layer in a Josephson junction (ξ_N), and the ratio of the local depairing current density of the grain boundary to the depairing current density of the superconductor: J_{DN}/J_{DSc}, given by equation (17). For angular averaged (A.A.), microcrystalline and nanocrystalline YBCO, we have taken the resistivity values from measurements in this work and assumed that the grain boundaries are 1 nm thick. For all other materials, we have again assumed that the grain boundaries are 1 nm thick normal grain boundaries, but that the resistivity is equal to the resistivity of the grains. For all materials, we have assumed that the Sommerfeld constant and the Fermi velocity are an angular average in the calculation of $J_{DN}(4.2\ \mathrm{K})/\langle J_{Dsc}(4.2\ \mathrm{K})\rangle$.

Material	$\rho_N\,(T_c)$ (Ω m)	γ (J m⁻³ K⁻²)	v_F (10⁵ m s⁻¹)	$\xi_{SClean}(0)$ (nm)	$\xi_{SDirty}(0)$ (nm)	$\dfrac{\xi_{SPippard}(0)}{\xi_{B_{c2}}(0)}$ (nm)	D_N (m² s⁻¹)	ξ_N(4.2 K) (nm)	$\dfrac{J_{DN}\,(4.2\ \mathrm{K})}{\langle J_{DSc}\,(4.2\ \mathrm{K})\rangle}$
NbTi	4.0×10^{-7} [127]	1.1×10^{3} [127]	2.0 [59, 127]	31	4.3	3.8 4.6	5.7×10^{-5}	6.4	0.28
Nb₃Sn	8.8×10^{-8} [16]	1.2×10^{3} [33]	0.60 [128]	4.6	6.3	2.7 3.3	2.4×10^{-4}	13	0.21
PbMo₆S₈	7.0×10^{-7} [34]	3.8×10^{2} [34]	0.40 [128]	4.0	4.5	2.1 2.4	9.2×10^{-5}	8.1	0.21
MgB₂ (A.A.)	1.0×10^{-6} [129]	1.5×10^{2} [130]	6.1 [131]	22	3.5	3.0 4.3	1.6×10^{-4}	10	0.28
YBa₂Cu₃O₇₋ₓ (ab-plane)	5.0×10^{-7}	2.0×10^{2} [132]	5.0 [56]	7.5	2.8	2.1 1.5	2.4×10^{-4}	13	0.16
YBa₂Cu₃O₇₋ₓ (A.A., 5 μm)	5.0×10^{-5}	2.0×10^{2} [132]	5.0 [56]	7.5	0.28	0.27 1.5	2.4×10^{-6}	1.3	0.077
YBa₂Cu₃O₇₋ₓ (Micro, 5 μm)	1.2×10^{-1}	2.0×10^{2} [132]	5.0 [56]	7.5	0.28	0.27 1.5	1.0×10^{-9}	0.027	10^{-35}
YBa₂Cu₃O₇₋ₓ (Nano, 100 nm)	8.2	2.0×10^{2} [132]	5.0 [56]	7.5	0.28	0.27 1.5	1.5×10^{-11}	0.0033	10^{-270}

layer. The largest uncertainties in calculating J_{DN} are associated with the values of the microscopic properties of the grain boundaries. We have simplified the analysis by assuming that grain boundary structures are not superconducting (i.e. $T_{cN} = 0$) and that we can use resistivity to characterise the difference between the microscopic properties of the grains and the grain boundaries. Grain boundaries are complex structures and one can expect that when their resistivity changes, their carrier concentration, effective width and scattering time all change. Our assumptions lead to $\xi_{NPippard}(T_{cS}) = \xi_{NDirty}(T_{cS})$ and

$$\xi_N(T) \approx \xi_{NDirty}(T_{cS})\left(\frac{T_{cS}}{T}\right)^{\frac{1}{2}} = \xi_{SDirty}(0)\left(\frac{\rho_S}{\rho_N}\frac{T_{cS}}{T}\right)^{\frac{1}{2}}. \quad (28)$$

As a starting point for calculating $\langle J_{DN}(0)\rangle$, in table 3 we have assumed that the grain boundary thicknesses in all the materials (i.e. d in equation (17)) is 1 nm. Equations (17) and (28) show that as the resistivity of the grain boundaries increases, ξ_N decreases and $\langle J_{DN}(0)\rangle$ is severely depressed. In the micro-crystalline YBCO materials of this work, the resistivity is more than three orders of magnitude higher than the grains, which by itself provides a straightforward explanation for the very low transport current densities we have experimentally measured. The calculations of $\langle J_{DN}(0)\rangle$ are particularly sensitive to the values of d and ξ_N. Once ξ_N is smaller than d, the exponential term in equation (17) dominates. In this regime, small increases in d produce very large reductions in $\langle J_{DN}(0)\rangle$. The resistivity of our nanocrystalline materials is even higher than the micro-crystalline values and $\langle J_{DN}(0)\rangle$ even lower. We note that these very high values of resistivity are beyond the Ioffe–Regel criterion (i.e. $k_F l < 1$ [85]). However, we conclude that even the straightforward analysis provided here demonstrates that the values of grain boundary resistivity we have measured in microcrystalline and nanocrystalline materials are sufficient to explain the low values of our transport J_c data.

5. Discussion

5.1. Micro- and nanocrystalline YBCO

We have found, using a combination of transport measurements and ac magnetic susceptibility measurements, that our nano- and microcrystalline YBCO can be considered to be high quality grains surrounded by non-superconducting highly resistive grain boundaries that limit transport J_c. The current densities within the grains are high and those across the grain boundaries low. We have adopted a pragmatic approach to the analysis of the grain boundaries in our samples and used angular averages for this strongly anisotropic material and ignored percolation. We have also adopted a simple two-component description of our materials as grains and grain boundaries and used an S-N-S description that assumes that the pinning is sufficiently strong along the grain boundaries that J_c is determined by the local depairing current density in the grain boundaries themselves. One can expect in superconducting materials there are a range of different length scales for the variations in composition, strain and physical

structure as well as electronic and phononic structure. Although it is reasonable for us to have assumed that grain boundary structures are not superconducting themselves in bulk form, finding the other characteristic microscopic properties of the grain boundaries (γ, v_F, l, n) will be a formidable challenge. Characterising bulk materials in thin film form proved difficult enough for the scientific community with the luxury of free-standing samples, or samples on insulators and data for parent bulk samples. Grain boundaries can be considered as internal surfaces. They bring the challenges of characterising a structure that is inhomogenous, is sandwiched between two grains, and is not available in bulk form [86]. Given the large effort it has taken to understand bulk materials, one can expect an even larger effort will be required for the local normal and superconducting properties of grain boundaries.

From a technological perspective, we would like to increase J_c in polycrystalline YBCO if at all possible. The [001] tilt boundaries in the literature have contact resistivities which vary from 2×10^{-14} Ωm^2 in the low angle bicrystal data [3], up to 10^{-11} Ωm^2 for 40° boundaries [87]. The average contact resistivities in our microcrystalline samples were 10^{-10} Ωm^2 and in the nanocrystalline samples 10^{-8} Ωm^2. Higher average contact resistivity values are expected in the polycrystalline samples than bicrystals because the misorientation angles are not limited to [001] tilt grain boundaries. We have modelled grain boundaries, as simple non-superconducting resistive layers. This ignores complexities such as the possibility that very low angle grain boundaries may have non-zero critical temperature and high angle grain boundaries may be ferromagnetic [62, 63], which in the G–L framework can be described using negative local critical temperatures. However, table 3 shows that even if we just apply our simple model, and reduce the grain boundary resistivity to be the same as the grains, the value of J_{DN}/J_{DSc} along the *ab*-plane is still 0.16, which is similar to that in the best YBCO tapes. For bulk YBCO with equal grain and grain boundary resistivity, J_{DN}/J_{DSc} is further reduced to 0.077. We may hope that faceted grain boundaries [88] may help but given the high grain boundary resistivities found at high angles in bicrystal data, it seems unlikely that grain boundary engineering will enable high J_c in polycrystalline YBCO. Grain boundary engineering such as Ca doping has successfully reduced grain boundary contact resistivity by over an order of magnitude and increased J_c by a factor of 6–7, however these results were on bicrystals preferentially doped at grain boundaries [5], thin film bicrystals [89] or multilayer films [90]. We consider it unlikely that one can reduce the grain boundary resistivity in polycrystalline materials to be less than that of the grains themselves and therefore that grain boundary engineering is unlikely to be successful in increasing J_c to technologically useful values, in randomly aligned polycrystalline YBCO.

5.2. Improving J_c in LTS and HTS high-field superconductors

The data in the second panel of figure 1 shows that in high fields, all technological superconductors have a large headroom

for improvement. In applied fields of half $B_{c2}(4.2\,\text{K})$, NbTi is only a few percent of its theoretical limit, and $Nb_3Sn(IT)$ produced using the internal tin route is only about 0.3% of its theoretical limit. Materials with the highest J_c/J_{DSc} values include commercial YBCO tape [28], thin film $Ba(FeCo)_2As_2$ [91] and Nb [12] that have been fabricated with no large-angle grain boundaries. Hence one can expect high J_D throughout the entire material, and strong pinning to be effective. It is unclear whether adding even more pinning will lead to further improvements, or whether the low angle grain boundaries or channels formed by contiguous strained and degraded material between pinning sites provide channels for flux flow and hence limit J_{DN}/J_{DSc} in these three materials. In addition to the thin film Ba-122 in figure 1, Ba-122 thin films with artificially engineered superlattices with strong pinning along the *ab*-plane and *c*-axis and improved J_c over a wide angular range [92] have been developed. Although untextured polycrystalline bulks and wires have achieved J_c of $10^9\,\text{Am}^{-2}$ at 0 T and 4.2 K, which is more than 10 times higher than other round untextured ferropnictide wires, it is still 10 times lower than the thin film materials [93]. The materials with markedly low J_c/J_{DSc} values include MgB_2 [94], $FeSe_{0.5}Te_{0.5}$ [95] and the A15 polycrystalline materials [96, 97]. Excellent polycrystalline, untextured MgB_2 can be produced cheaply through solid state reactions [98–101], as can $FeSe_{0.5}Te_{0.5}$ through sintering [102] or powder-in-tube process [103]. However, such $FeSe_{0.5}Te_{0.5}$ materials achieve J_c values of $10^7\,\text{Am}^{-2}$ at 0 T and 4.2 K, which are two orders of magnitude lower than the tape sample in figure 1. After Nb_3Sn was discovered in 1954 [104], materials for magnets were fabricated with J_c values of $1.5 \times 10^9\,\text{Am}^{-2}$ at 8.8 T in 1961 [105]. By 1990, J_c values of $2.2 \times 10^9\,\text{Am}^{-2}$ at 11 T were achieved [106] and now state-of-the-art values are approximately $8 \times 10^9\,\text{Am}^{-2}$ at 11 T. Improvements in J_c are hard-earned and have enabled technological applications above 10 T including high-field MRI, particle accelerator magnets and fusion energy. However, an improvement in J_c by an order of magnitude over 50 years does not seem very large in the context of a headroom of nearly 3 orders of magnitude between J_c and the theoretical upper limit J_{DSc}. If flux flow along channels rather than pinning in the grains are the problem, equation (17) suggests high grain boundary resistivity and/or wide grain boundaries are responsible. The resistivity of Nb_3Sn and the other A15 intermetallics has been studied extensively. Very large changes in resistivity have been found in Nb_3Sn and V_3Si with relatively small changes in composition [107]. For binary Nb_3Sn, $\rho_N = 4 \times 10^{-8}\,\Omega\text{m}$ for 25 at% Sn and $\rho_N = 4 \times 10^{-7}\,\Omega\text{m}$ for 24.5 at% Sn. In a series of nanocrystalline HIP'ed Nb_3Sn fabricated in our group, materials with 120 nm grain size and $T_c = 17.4\,\text{K}$ and $B_{c2}(0) = 30\,\text{T}$, $J_c = 3 \times 10^9\,\text{Am}^{-2}$ at 0 T and 5 K, $J_c = 7 \times 10^8\,\text{Am}^{-2}$ at 6 T and 5 K, were found to have resistivity values of $\rho_N = 6 \times 10^{-7}\,\Omega\text{m}$ [108]. When the grain size was reduced to 20 nm, T_c reduced to 10 K and ρ_N increased to $2 \times 10^{-6}\,\Omega\text{m}$. When the grain size was below 10 nm, T_c was below 2 K and ρ_N increased to $4 \times 10^{-6}\,\Omega\text{m}$ [109]. These nanocrystalline results show that very high resistivity values can occur in Nb_3Sn and that a non-superconducting width for the grain boundaries of 3 nm in Nb_3Sn polycrystalline materials is not unreasonable. The quality of our

nanocrystalline Nb_3Sn materials may simply have been poor, but the sustained low J_c/J_{DSc} values in state-of-the-art materials may point to a more fundamental grain boundary problem. There are other factors may also help explain why the effective width of non-superconducting grain boundaries are large in A15 compounds. Band structure calculations point to the density of states at the Fermi level being determined by the one-dimensional chains of Nb atoms [107, 110]. Variable strain measurements show that a strain as low as 1% significantly depresses T_c [97, 111, 112]. Calculations using equation (17) show that for Nb_3Sn, low values of $J_{DN}(4.2\,\text{K})/J_{DSc}(4.2\,\text{K})$ of just 0.2% can occur, when the grain boundary width is 3 nm and $\rho_N = 4 \times 10^{-6}\,\Omega\text{m}$. It follows that improvement in the J_c of Nb_3Sn can be achieved if the grain boundaries are improved or removed. However, the properties of the grains and the grain boundaries cannot be considered completely decoupled. If we improve the connectivity by lowering the resistivity of the grain boundaries, although we increase the local depairing current in the grain boundaries, we can expect to decrease the surface pinning that restrains the fluxons within the superconducting grains. Hence, we may need to add strong pinning sites into the grains themselves. Whether the improvements would be commercially viable is beyond the scope of this paper.

6. Conclusion

Micro- and nanocrystalline YBCO samples were fabricated in order to study the nature of grain boundaries. Detailed magnetic data enabled us to measure and distinguish hysteretic screening currents, limited to within the grains, from transport currents that cross grain boundaries and conclude that the magnetisation J_c is at least 10^5–10^6 times larger than transport J_c for both our micro- and nanocrystalline materials. Using resistivity data and considering the polycrystalline material as S-N-S junctions, we have shown that high resistivity in the grain boundaries is enough by itself to reduce the local depairing current density of the grain boundaries and hence limit the transport J_c. For microcrystalline materials, transport J_c on the order of $10^5\,\text{Am}^{-2}$ was measured. In our nanocrystalline samples, we found there were no intergranular currents through our samples except for just one, in which J_c was reduced by at least 10^9 compared to commercial tapes. This work has provided a quantitative description of grain boundaries that we hope can help provide a framework to extend our characterisation of grain boundaries from those in model systems and bicrystals, to those in technologically-important high-field superconducting materials that are used in commercial applications. It provides calculations that identify when grain boundaries are so resistive they limit J_c in polycrystalline materials. Grain boundaries in polycrystalline technological materials are complex and inhomogeneous. We expect a more complete treatment to consider percolative effects and to provide more sophisticated measurements of local grain boundary properties.

Acknowledgments

Appendix

The temperature dependence of the depairing current density for a superconductor ($J_{DSc}(T)$), as listed in table 1 is calculated as shown below. Our approach was broadly either to find expressions for the G–L penetration depth (λ), the G–L coherence length (ξ) and T_c directly from the literature or to find the upper critical field ($B_{c2}(T)$) and lower critical field ($B_{c1}(T)$) at any temperature from the literature and use well known temperature dependencies for these critical fields to calculate λ and ξ. In table 1, we have shown values of the critical fields and length scales at 0 K.

A.1. Calculation of J_{DSc}^{ab} in zero field

First we consider the G–L expression for the depairing current density of an anisotropic superconducting material such as YBCO or an isotropic superconductor. When the current is in the *ab* plane, J_{DSc}^{ab} is given by:

$$J_{DSc}^{ab}(T) = \frac{\Phi_0}{3\sqrt{3}\,\pi\mu_0\lambda_{ab}^2(T)\xi_{ab}(T)}, \tag{29}$$

where Φ_0 is the flux quantum, $\lambda_{ab}(T)$ is the G–L penetration depth and $\xi_{ab}(T)$ is the G–L coherence length. Since there is no general theoretical expressions for $B_{c2}(T)$, we use an empirical equation of the form:

$$B_{c2}^c(T) = B_{c2}^c(0)(1 - (T/T_c)^\nu). \tag{30}$$

Note in equation (30) that when the applied magnetic field points in the *c*-axis direction, the relevant length scale is the G–L coherence length in the *ab*-plane. We can differentiate equation (30) with respect to T to obtain:

$$\left.\frac{\partial B_{c2}^c(T)}{\partial T}\right|_{T\approx T_c} = -\frac{\nu}{T_c}B_{c2}^c(0). \tag{31}$$

We use the G–L equation for $B_{c2}(T)$ (correct only for $T \approx T_c$) [113]:

$$B_{c2}^c(T) = \left.\frac{\Phi_0}{2\pi\xi_{ab}^2(T)}\right|_{T\approx T_c} \tag{32}$$

and the G–L expression for the G–L coherence length $\xi_{ab}(T)$, which is generally taken to be true for all temperatures, of the form:

$$\xi_{ab}(T) = \xi_{ab}(0)(1 - (T/T_c))^{-1/2}. \tag{33}$$

We can differentiate equation (32) with respect to T to obtain:

$$\left.\frac{\partial B_{c2}^c(T)}{\partial T}\right|_{T\approx T_c} = \frac{\Phi_0}{2\pi\xi_{ab}^2(0)}\left(-\frac{1}{T_c}\right). \tag{34}$$

From equations (31) and (34) we have:

$$\xi_{ab}^2(0) = \frac{\Phi_0}{2\pi B_{c2}^c(0)}\frac{1}{\nu}. \tag{35}$$

Substituting this equation into equation (33), we have:

$$\xi_{ab}^2(T) = \frac{\Phi_0}{2\pi B_{c2}^c(0)}\frac{1}{\nu}\frac{1}{1-(T/T_c)} \tag{36}$$

Substituting equation (30) into (36) leads to:

$$\xi_{ab}^2(T) = \frac{\Phi_0}{2\pi B_{c2}^c(T)}\frac{1}{\nu}\frac{1-(T/T_c)^\nu}{1-(T/T_c)}. \tag{37}$$

The temperature dependence of λ in the *ab*-plane can be calculated in a similar way using:

$$B_{c1}^c(T) = B_{c1}^c(0)(1 - (T/T_c)^\eta), \tag{38}$$

where η has been taken to have a value of 2 for all superconductors. This can be differentiated to give:

$$\left.\frac{\partial B_{c1}^c(T)}{\partial T}\right|_{T\approx T_c} = B_{c1}^c(0)\left(-\frac{\eta}{T_c}\right). \tag{39}$$

We also use the G–L relation for the G–L penetration depth, valid at all temperatures:

$$\lambda_{ab}(T) = \lambda_{ab}(0)(1 - (T/T_c))^{-1/2} \tag{40}$$

and the G–L relation for $B_{c1}^c(T)$ [113]:

$$\begin{aligned}B_{c1}^c(T) &= \frac{\Phi_0}{4\pi\lambda_{ab}^2(T)}\left\{\ln\left(\frac{\lambda_{ab}(T)}{\xi_{ab}(T)}\right) + 0.5\right\}\\ &= \frac{\Phi_0}{4\pi\lambda_{ab}^2(T)}\left\{\ln\left(\frac{\lambda_{ab}(0)}{\xi_{ab}(0)}\right) + 0.5\right\},\end{aligned} \tag{41}$$

which can be differentiated to give:

$$\left.\frac{\partial B_{c1}^c(T)}{\partial T}\right|_{T\approx T_c} = \frac{\Phi_0}{4\pi\lambda_{ab}^2(0)}\left(-\frac{1}{T_c}\right)\left\{\ln\left(\frac{\lambda_{ab}(0)}{\xi_{ab}(0)}\right) + 0.5\right\}. \tag{42}$$

Combining equations (39) and (42) leads to:

$$\lambda_{ab}^2(0) = \frac{\Phi_0}{4\pi\eta B_{c1}^c(0)}\left\{\ln\left(\frac{\lambda_{ab}(0)}{\xi_{ab}(0)}\right) + 0.5\right\}. \tag{43}$$

Combining equations (38), (40) and (43) gives $\lambda_{ab}(T)$:

$$\lambda_{ab}^2(T) = \frac{\Phi_0}{4\pi\eta}\frac{1-(T/T_c)^\eta}{B_{c1}^c(T)(1-(T/T_c))}\left\{\ln\left(\frac{\lambda_{ab}(0)}{\xi_{ab}(0)}\right) + 0.5\right\}. \tag{44}$$

Equations (37) and (44) can be substituted into equation (29) to calculate $J_{\mathrm{Dsc}}^{ab}(T)$.

A.2. Calculation of J_{DSc}^{c} in zero field

For anisotropic materials, we can also calculate the depairing current density when the current is flowing in the c-axis direction (J_{DSc}^{c}), given by:

$$J_{\mathrm{DSc}}^{c}(T) = \frac{\Phi_0}{3\sqrt{3}\,\pi\mu_0 \lambda_c^2(T)\xi_c(T)}. \tag{45}$$

Using the general result for anisotropic superconductors [57]:

$$\lambda_{ab}\xi_{ab} = \lambda_c\xi_c, \tag{46}$$

we have:

$$J_{\mathrm{DSc}}^{c}(T) = J_{\mathrm{DSc}}^{ab}(T)\frac{\lambda_{ab}(0)}{\lambda_c(0)} = J_{\mathrm{DSc}}^{ab}(T)\frac{\xi_c(0)}{\xi_{ab}(0)}. \tag{47}$$

The G–L relation for $B_{c2}^{ab}(T)$ is [113]:

$$B_{c2}^{ab}(T) = \frac{\Phi_0}{2\pi\xi_c(T)\xi_{ab}(T)}\bigg|_{T\approx T_c} \tag{48}$$

and the scaling with temperature is given by:

$$B_{c2}^{ab}(T) = B_{c2}^{ab}(0)(1-(T/T_c)^{\nu}). \tag{49}$$

Similar to the methods described above for current flowing in the ab-plane, by combining the derivatives of equations (48) and (49) we find:

$$\xi_c(0) = \frac{\Phi_0}{2\pi B_{c2}^{ab}(0)\xi_{ab}(0)}\frac{1}{\nu} = \frac{\Phi_0}{2\pi B_{c2}^{ab}(T)\xi_{ab}(0)}\frac{1}{\nu}\left(1-\left(\frac{T}{T_c}\right)^{\nu}\right), \tag{50}$$

where $\xi_{ab}(0)$ can be obtained from equation (35), and $\xi_c(T)$ can be found using:

$$\xi_c(T) = \xi_c(0)(1-(T/T_c))^{-1/2}. \tag{51}$$

Finally, $\lambda_c(T)$ can be found given $\xi_{ab}(T)$, $\xi_c(T)$ and $\lambda_{ab}(T)$ using equation (46). Hence we can calculate the values necessary to produce (45) and figure 1 [13–25].

References

[1] Schauer W and Schelb W 1981 Improvement of Nb$_3$Sn high field critical current by a two-stage reaction *IEEE Trans. Magn.* **17** 374–7

[2] Carty G J and Hampshire D P 2008 Visualising the mechanism that determines the critical current density in polycrystalline superconductors using time-dependent Ginzburg–Landau theory *Phys. Rev.* B **77** 172501

[3] Dimos D, Chaudhari P and Mannhart J 1990 Superconducting transport properties of grain boundaries in YBa$_2$Cu$_3$O$_7$ bicrystals *Phys. Rev.* B **41** 4038–49

[4] Ekin J W *et al* 1987 Evidence for weak link and anisotropy limitations on the transport critical current in bulk polycrystalline Y$_1$Ba$_2$Cu$_3$O$_x$ *J. Appl. Phys.* **62** 4821–8

[5] Cheng C H and Zhao Y 2007 Repair of grain boundary by preferential-doping in YBa$_2$Cu$_3$O$_{7-y}$ *Physica* C **463** 174–7

[6] Ransley J H T *et al* 2004 The normal-state resistivity of grain boundaries in YBa$_2$Cu$_3$O$_{7-\delta}$ *Appl. Phys. Lett.* **84** 4089–91

[7] Graser S, Hirschfeld P J, Kopp T, Gutser R, Andersen B M and Mannhart J 2010 How grain boundaries limit supercurrents in high-temperature superconductors *Nat. Phys.* **6** 609

[8] Carty G J and Hampshire D P 2013 The critical current density of an SNS junction in high magnetic fields *Supercond. Sci. Technol.* **26** 065007

[9] Likharev K K 1979 Superconducting weak links *Rev. Mod. Phys.* **51** 102–59

[10] Babcock S E and Vargas J L 1995 The nature of grain boundaries in the high-T$_c$ superconductors *Annu. Rev. Mater. Sci.* **25** 193–222

[11] SuperPower-Furukawa 2013 SuperPower 2 G HTS Coated Conductors, (www.superpower-inc.com/content/2g-hts-wire)

[12] Dinner R B, Robinson A P, Wimbush S C, MacManus-Driscoll J L and Blamire M G 2011 Depairing critical current achieved in superconducting thin films with through-thickness arrays of artificial pinning centers *Supercond. Sci. and Technol.* **24** 055017

[13] Lee P J and Larbalestier D C On-Line Master J_c Plots, (http://magnet.fsu.edu/magnettechnology/research/asc/plots.html)

[14] Gauzzi A *et al* 2000 Very high resolution measurement of the penetration depth of superconductors by a novel single-coil inductance technique *Rev. Sci. Instrum.* **71** 2147–53

[15] Neuringer L J and Shapira Y 1966 Effect of spin-orbit scattering on the upper critical field of high-field superconductors *Phys. Rev. Lett.* **17** 81–4

[16] Orlando T P, McNiff E J, Foner S and Beasley M R 1979 Critical fields, Pauli paramagnetic limiting, and material parameters of Nb$_3$Sn and V$_3$Si *Phys. Rev.* B **19** 4545–61

[17] Finnemore D K, Ostenson J E, Bud'ko S L, Lapertot G and Canfield P C 2001 Thermodynamic and transport properties of superconducting Mg^{10}B$_2$ *Phys. Rev. Lett.* **86** 2420–2

[18] Lyard L *et al* 2003 Upper critical magnetic fields in single crystal MgB$_2$ *Supercond. Sci. Technol.* **16** 193–8

[19] Zheng D *et al* 1994 Magnetic susceptibilities, critical fields, and critical currents of Co- and Zn-doped YBa$_2$Cu$_3$O$_7$ *Phys. Rev.* B **49** 1417–26

[20] Sekitani T, Miura N, Ikeda S, Matsuda Y H and Shiohara Y 2004 Upper critical field for optimally-doped YBa$_2$Cu$_3$O$_{7-\delta}$ *Physica* B **346–347** 319–24

[21] Ri H C *et al* 1994 Nernst, seebeck, and Hall effects in the mixed state of YBa$_2$Cu$_3$O$_{7-d}$ and Bi$_2$Sr$_2$CaCu$_2$O$_{8+x}$ thin films: a comparative study *Phys. Rev.* B **50** 3312–29

[22] Golovashkin A I *et al* 1991 Low temperature direct measurements of H_{c2} in HTSC using megagauss magnetic fields *Physica* C **185** 1859–60

[23] Li Q, Suenaga M, Gohng J, Finnemore D K, Hikata T and Sato K 1992 Reversible magnetic properties of c-axis-oriented superconducting Bi$_2$Sr$_2$Ca$_2$Cu$_3$O$_{10}$ *Phys. Rev.* B **46** 3195–8

[24] Matsubara I, Tanigawa H, Ogura T, Yamashita H, Kinoshita M and Kawai T 1992 Upper critical field and anisotropy of the high-T$_c$ Bi$_2$Sr$_2$Ca$_2$Cu$_3$O$_x$ phase *Phys. Rev.* B **45** 7414–7

[25] Larbalestier D C, Gurevich A, Feldmann D M and Polyanskii A 2001 High-T$_c$ superconducting materials for electric power applications *Nature* **414** 368–77

[26] Ando Y *et al* 1999 Resistive upper critical fields and irreversibility lines of optimally doped high-T$_c$ cuprates *Phys. Rev.* B **60** 12475–9

[27] Chen B *et al* 2007 Two-dimensional vortices in superconductors *Nat. Phys.* **3** 239–42

[28] Larbalestier D C *et al* 2014 Isotropic round-wire multifilament cuprate superconductor for generation of magnetic fields above 30 T *Nat. Mater.* **13** 375–81

[29] Raine M J, Keys S A and Hampshire D P 2017 *Characterisation of the Transport Critical Current Density for Conductor Applications* (London: Taylor and Francis)

[30] Lee T S, Jenkins I, Surrey E and Hampshire D P 2015 Optimal design of a toroidal field magnet system and cost of electricity implications for a tokamak using high temperature superconductors *Fusion Eng. Des.* **98–99** 1072–5

[31] Sunwong P, Higgins J S, Tsui Y, Raine M J and Hampshire D P 2013 The critical current density of grain boundary channels in polycrystalline HTS and LTS superconductors in magnetic fields *Supercond. Sci. Technol.* **26** 095006

[32] Hampshire D P and Niu H J 2002 Patent—nanocrystalline superconductors *International Patent Number* WO03/ 094251 A2 UK Patent Office

[33] Taylor D M J, Al-Jawad M and Hampshire D P 2008 A new paradigm for fabricating bulk high-field superconductors *Supercond. Sci. Technol.* **21** 125006

[34] Niu H J and Hampshire D P 2003 Disordered nanocrystalline superconducting $PbMo_6S_8$ with very large upper critical field *Phys. Rev. Lett.* **91** 027002

[35] Xiang J Y, Fleck C and Hampshire D P 2008 Bulk nanocrystalline superconducting $YBa_2Cu_3O_{7-x}$ *J. Phys.: Conf. Ser.* **97** 012237

[36] Hamrita A *et al* 2014 Superconducting properties of polycrystalline $YBa_2Cu_3O_{7-d}$ prepared by sintering of ball-milled precursor powder *Ceram. Int.* **40** 1461

[37] Xu X L, Guo J D, Wang Y Z and Sozzi A 2002 Synthesis of nanoscale superconducting YBCO by a novel technique *Physica* C **371** 129–32

[38] Shi Y *et al* 2012 Synthesis of $YBa_2Cu_3O_{7-\delta}$ and Y_2BaCuO_5 nanocrystalline powders for YBCO superconductors using carbon nanotube templates *ACS Nano* **6** 5395–403

[39] Shi Y *et al* 2010 Batch-processed GdBCO–Ag bulk superconductors fabricated using generic seeds with high trapped fields *Physica* C **470** 685–8

[40] Zhai W, Shi Y, Durrell J H, Dennis A R, Zhang Z and Cardwell D A 2015 Processing and properties of bulk Y−Ba−Cu−O superconductors fabricated by top seeded melt growth from precursor pellets containing a graded CeO_2 composition *Cryst. Growth Des.* **15** 907–14

[41] Yan M F, Barns R L, Obryan H M, Gallagher P K, Sherwood R C and Jin S 1987 Water interaction with the superconducting $YBa_2Cu_3O_7$ phase *Appl. Phys. Lett.* **51** 532–4

[42] Barns R L and Laudise R A 1987 Stability of superconducting $YBa_2Cu_3O_7$ in the presence of water *Appl. Phys. Lett.* **51** 1373–5

[43] Simoneau M, L'Esperamce G and Schulz R 1994 Formation by ball milling and recrystallization of Y−Ba−Cu−O nanocrystalline phases *J. Appl. Phys.* **76** 136

[44] Liang R, Bonn D A and Hardy W N 2006 Evaluation of CuO_2 plane hole doping in $YBa_2Cu_3O_{6+x}$ single crystals *Phys. Rev.* B **73** 180505

[45] Schwarz R B and Petrich R R 1988 Calorimetry study of the synthesis of amorphous Ni–Ti alloys by mechanical alloying *J. Less Common Met.* **140** 171

[46] Sestak J 1992 Phase-diagrams in CuO_x based superconductors *Pure Appl. Chem.* **64** 125–36

[47] Vajpei A and Upadhyaya G (ed) 1992 *Powder Processing of High T_c Oxide Superconductors* (Switzerland: Trans Tech)

[48] Aselage T and Keefer K 1988 Liquidus relations in Y–Ba–Cu oxides *J. Mater. Res.* **3** 1279–91

[49] Quantum Design 2004 PPMS resistivity option user's manual *PPMS Hardware and Options Manual* (San Diego: Quantum Design)

[50] 2016 EM Electronics, DC Nanovolt Amplifier Model A10, (http://emelectronics.co.uk/a10.html), 19 September

[51] Dimos D, Chaudhari P, Mannhart J and LeGoues F K 1988 Orientation dependence of grain-boundary critical currents in $YBa_2Cu_3O_{7-\delta}$ bicrystals *Phys. Rev. Lett.* **61** 219–22

[52] Laby K 1995 *Tables of Physical & Chemical Constants* 16th edn (The National Physical Laboratory)

[53] Quantum Design 2004 PPMS ACMS user's manual *PPMS Hardware and Options Manual* (San Diego: Quantum Design) pp 1–3

[54] Pusceddu E and Hampshire D P 2012 Nanocrystalline superconducting islands of Nb_3Ge in a resistive grain boundary matrix with a bulk critical temperature of 12 K *Supercond. Sci. Technol.* **25** 115014

[55] Shoenberg D 1952 *Superconductivity* (Cambridge: Cambridge University Press)

[56] Seidel P, Grajar M, Plecenik A and Hlubina R 1996 Superconducting parameters of YBCO and BSCCO from 'tunneling' spectroscopy *Physica* B **218** 224–7

[57] Clem J R 1998 Anisotropy and two-dimensional behaviour in the high-temperature superconductors *Supercond. Sci. Technol.* **11** 909–14

[58] Klemm R A and Clem J R 1980 Lower critical field of an anisotropic type-II superconductor *Phys. Rev.* B **21** 1868–75

[59] Poole C P, Farach H A and Creswick R J 1995 *Superconductivity* (San Diego, CA: Academic)

[60] Gomathi A S, Sundaresan A and Rao C N R 2007 Room-temperature ferromagnetism in nanoparticles of superconducting materials *Solid State Commun.* **142** 685–8

[61] Hasanain S K A, Akhtar N and Mumtaz A 2011 Particle size dependence of the superconductivity and ferromagnetism in YBCO nanoparticles *J. Nanopart. Res.* **13** 1953–60

[62] Straumal B B *et al* 2015 Grain boundaries as a source of ferromagnetism and increased solubility of Ni in nanograined ZnO *Rev. Adv. Mater. Sci.* **41** 61–71

[63] Straumal B B *et al* 2016 Ferromagnetic behaviour of ZnO: the role of grain boundaries *Beilstein J. Nanotechnol.* **7** 1936–47

[64] Campbell A M 1969 The response of pinned flux vortices to low-frequency fields *J. Phys. C: Solid State Phys.* **2** 1492–501

[65] Shimizu E and Ito D 1989 Critical current density obtained from particle-size dependence of magnetization in $YBa_2Cu_3O_{7-\delta}$ powders *Phys. Rev.* B **39** 2921–3

[66] Bennemann K H and Ketterson J B 2004 *The Physics of Superconductors: Vol. II: Superconductivity in Nanostructures, High-T_c and Novel Superconductors, Organic Superconductors* (Berlin: Springer)

[67] Loram J W, Mirza K A, Cooper J R, Liang W Y and Wade J M 1994 Electronic specific heat of $YBa_2Cu_3O_{6+x}$ from 1.8 to 300 K *J. Supercond.* **7** 243–9

[68] Gerbstein Y M, Timoshchenko N E and Chudnovskii F A 1989 Measurement of electron density of states at the Fermi level in YBCO by means of an 'oxygen pump' *Physica* C **162** 961–2

[69] Yeh N C *et al* 2002 Investigating the pairing state of cuprate superconductors via quasiparticle tunneling and spin injection *Physica* C **367** 174–80

[70] Buschow K H J 2005 *Concise Encyclopedia of Magnetic and Superconducting Materials* (London: Elsevier Science)

[71] Hsiang T Y and Finnemore D K 1980 Superconducting critical currents for thick, clean superconductor-normal-metal-superconductor junctions *Phys. Rev.* B **22** 154–63

[72] Lacquaniti V, Gonzini S, Maggi S, Monticne E, Steni R and Andreone D 1999 Nb-based SNS junctions with Al and TaO_x barriers for a programmable Josephson voltage standard *IEEE Trans. Appl. Supercond.* **9** 4245–8

[73] Wang R F, Zhao S P, Chen G H and Yang Q S 2000 Magnetic penetration depth in Nb/Al and Nb/Cu superconducting proximity bilayers *Phys. Rev.* B **62** 11793–801

[74] Clarke J 1969 Supercurrents in lead-copper-lead sandwiches *Proc. R. Soc.* A **308** 447–71

[75] Bedard F and Meissner H 1956 Measurements of contact resistance between normal and superconducting metals *Phys. Rev.* **101** 26–30

[76] Forrester M G, Talvacchio J, Gavaler J R, Rooks M and Lindquist J 1991 Fabrication and characterization of $YBa_2Cu_3O_7/Au/YBa_2Cu_3O_7$ Josephson junctions *IEEE Trans. Magn.* **27** 3098–101

[77] Tsui Y, Surrey E and Hampshire D P 2016 Soldered Joints— an essential component of demountable high temperature superconducting fusion magnets *Supercond. Sci. Technol.* **290** 075005

[78] Wu J Z *et al* 1991 Anisotropic properties of the high-quality epitaxial $YBa_2Cu_3O_{7-d}$ (110) thin film *Phys. Rev.* B **44** 12643–6

[79] Edman L, Sundqvist B, McRae E and Litvin-Staszewska E 1998 Electrical resistivity of single-crystal graphite under pressure: an anisotropic three-dimensional semimetal *Phys. Rev.* B **57** 6227–30

[80] Entegris Properties and Characteristics of Graphite For the semiconductor industry (https://entegris.com/resources/ assets/6205-7329-0513.pdf)

[81] Vanderbemden P *et al* 1999 Intragranular and intergranular superconducting properties of bulk melt-textured YBCO *IEEE Trans. Appl. Supercond.* **9** 2308–11

[82] Zhu Y, Suenaga M, Xu Y, Sabatini R L and Moodenbaugh A R 1989 Observation of twin boundary layers in pure and alloyed $YBa_2Cu_3O_{7-\delta}$ *Appl. Phys. Lett.* **54** 374–6

[83] Hilgenkamp H and Mannhart J 2002 Grain boundaries in high-T_c superconductors *Rev. Mod. Phys.* **74** 485–549

[84] Ashcroft N W and Mermin N D 1976 *Solid State Physics* (Philadelphia: Sanders College Publishing)

[85] Mark R G, Adkins C J, Haim B and Ralph R 1998 Experimental study of the Ioffe–Regel criterion for amorphous indium oxide films *J. Phys.: Condens. Matter* **10** 809

[86] Jamtveit B and Meakin P 1999 *Growth, Dissolution, and Pattern Formation in Geosystems Pauli is Quoted as Saying 'God Made the Bulk; Surfaces were Invented by the Devil'* (London: Chapman and Hall) p 291

[87] Mannhart J and Hilgenkamp H 1999 Interfaces involving complex superconductors *Physica* C **317–318** 383–91

[88] Tsu I F, Wang J-L, Kaiser D L and Babcock S E 1998 A comparison of grain boundary topography and dislocation network structure in bulk-scale [001] tilt bicrystals of $Bi_2Sr_2CaCu_2O_{8+x}$ and $YBa_2Cu_3O_{7-\delta}$ *Physica* C **306** 163–87

[89] Schmehl A *et al* 1999 Doping-induced enhancement of the critical currents of grain boundaries in $YBa_2Cu_3O_{7-d}$ *Europhys. Lett.* **47** 110–5

[90] Hammerl G *et al* 2000 Enhanced supercurrent density in polycrystalline $YBa_2Cu_3O_{7-d}$ at 77 K from calcium doping of grain boundaries *Nature* **407** 162–4

[91] Tarantini C *et al* 2014 Development of very high J_c in $Ba(Fe_{1-x}Co_x)_2As_2$ thin films grown on CaF_2 *Sci. Rep.* **4** 7305

[92] Lee S *et al* 2013 Artificially engineered superlattices of pnictide superconductors *Nat. Mater.* **12** 392–6

[93] Weiss J D *et al* 2012 High intergrain critical current density in fine-grain $(Ba_{0.6}K_{0.4})Fe_2As_2$ wires and bulks *Nat. Mater.* **11** 682–5

[94] Li G Z *et al* 2013 Effects of carbon concentration and filament number on advanced internal Mg infiltration-processed MgB_2 strands *Supercond. Sci. Technol.* **26** 095007

[95] Si W *et al* 2011 Iron-chalcogenide $FeSe_{0.5}Te_{0.5}$ coated superconducting tapes for high field applications *Appl. Phys. Lett.* **98** 262509

[96] Lu X F, Pragnell S and Hampshire D P 2007 Small reversible axial-strain window for critical current in both compression and tension for a high performance Nb_3Sn superconducting strand *Appl. Phys. Lett.* **91** 132512

[97] Taylor D M J and Hampshire D P 2005 The scaling law for the strain dependence of the critical current density in Nb_3Sn superconducting wires *Supercond. Sci. Technol.* **18** S241–52

[98] Tomoyuki N, Tomohisa S and Hiroyuki F 2012 Trapped magnetic field and vortex pinning properties of MgB_2 superconducting bulk fabricated by a capsule method *Supercond. Sci. Technol.* **25** 095012

[99] Muralidhar M, Ishihara A, Suzuki K, Fukumoto Y, Yamamoto Y and Tomita M 2013 Optimization of the fabrication process for high trapped field MgB_2 bulks *Physica* C **494** 85–8

[100] Kambara M *et al* 2001 High intergranular critical currents in metallic MgB_2 superconductor *Supercond. Sci. Technol.* **14** L5

[101] Larbalestier D *et al* 2001 Strongly linked current flow in polycrystalline forms of the superconductor MgB_2 *Nature* **410** 186–9

[102] Palenzona A *et al* 2012 A new approach for improving global critical current density in $Fe(Se_{0.5}Te_{0.5})$ polycrystalline materials *Supercond. Sci. Technol.* **25** 115018

[103] Ozaki T *et al* 2012 Fabrication of binary FeSe superconducting wires by diffusion process *J. Appl. Phys.* **111** 112620

[104] Matthias B T, Geballe T H, Geller S and Corenzwit E 1954 Superconductivity of Nb_3Sn *Phys. Rev.* **95** 1435

[105] Kunzler J E 1961 Superconductivity in high magnetic fields at high current densities *Rev. Mod. Phys.* **33** 501–9

[106] Godeke A, den Ouden A, Nijhuis A and ten Kate H H J 2008 State of the art powder-in-tube niobium–tin superconductors *Cryogenics* **48** 308–16

[107] Evetts J (ed) 1992 *Concise Encyclopedia of Magnetic and Superconducting Materials* (*Advances in Materials Science and Engineering*) (Oxford: Pergamon)

[108] King M B 2006 Mechanically milled bulk nanocrystalline NB3Sn with imprfov ed superconducting properties in high magnetic fields *PhD Thesis* Durham University

[109] Xiang J, King M B and Hampshire D 2010 private communication

[110] Rullier-Albenque F and Quere Y 1981 An experimental argument—in Nb3Ge—for the Labbe–Barisic–Friedel theory of A-15 superconductors *Phys. Lett.* A **81** 232–4

[111] Cheggour N and Hampshire D P 2002 The unified strain and temperature scaling law for the pinning force density of bronze-route Nb_3Sn wires in high magnetic fields *Cryogenics* **42** 299–309

[112] Keys S A and Hampshire D P 2003 A scaling law for the critical current density of weakly and strongly-coupled superconductors, used to parameterise data from a technological Nb_3Sn strand *Supercond. Sci. Technol.* **16** 1097–108

[113] Burns G 1992 Superconducting properties *High-Temperature Superconductivity* (New York: Academic) pp 156–7

[114] Williamson S J 1970 Bulk upper critical field of clean type-II superconductors: V and Nb *Phys. Rev.* B **2** 3545–56

[115] Zheng D N, Ramsbottom H D and Hampshire D P 1995 Reversible and irreversible magnetization of the Chevrel-phase superconductor $PbMo_6S_8$ *Phys. Rev.* B **52** 12931–8

[116] Keys S A, Koizumi N and Hampshire D P 2002 The strain and temperature scaling law for the critical current density of a jelly-roll Nb_3Al strand in high magnetic fields *Supercond. Sci. Technol.* **15** 991–1010

[117] Hampshire D P, Jones H and Mitchell E W J 1985 An in-depth characterisation of (NbTa)$_3$Sn filamentary superconductor *IEEE Trans. Magn.* **21** 289–92

[118] Godeke A, Jewell M C, Fischer C M, Squitieri A A, Lee P J and Larbalestier D C 2005 The upper critical field of filamentary Nb$_3$Sn conductors *J. Appl. Phys.* **97** 093909

[119] Guritanu V *et al* 2004 Specific heat of Nb3Sn: the case for a second energy gap *Phys. Rev.* B **70** 184526

[120] Xu M *et al* 2001 Anisotropy of superconductivity from MgB$_2$ single crystals *Appl. Phys. Lett.* **79** 2779–81

[121] Hänisch J *et al* 2015 High field superconducting properties of Ba(Fe$_{1-x}$Co$_x$)$_2$As$_2$ thin films *Sci. Rep.* **5** 17363

[122] Wu D *et al* 2010 Superfluid density of from optical experiments *Physica C: Superconductivity* **470** (Suppl. 1) S399–400

[123] Braithwaite D, Lapertot G, Knafo W and Sheikin I 2010 Evidence for anisotropic vortex dynamics and pauli limitation in the upper critical field of FeSe$_{1-x}$Te$_x$ *J. Phys. Soc. Japan* **79** 053703

[124] Bendele M *et al* 2010 Anisotropic superconducting properties of single-crystalline FeSe$_{0.5}$Te$_{0.5}$ *Phys. Rev.* B **81** 224520

[125] Mitra S, Cho J H, Lee W C, Johnston D C and Kogan V G 1989 Magnetic field penetration depth of polycrystalline (Y, Gd)Ba$_2$Cu$_3$O$_7$, grain-aligned YBa$_2$Cu$_3$O$_7$, and single-crystal Bi$_2$Sr$_2$CaCu$_2$O$_8$ *Phys. Rev.* B **40** 2674–7

[126] Miu L, Wagner P, Frey U, Hadish A, Miu D and Adrian H 1995 Vortex unbinding and layer decoupling in epitaxial Bi$_2$Sr$_2$Ca$_2$Cu$_3$O$_{10+\delta}$ films *Phys. Rev.* B **52** 4553–8

[127] Collings E W 1986 Applied superconductivity, metallurgy, and physics of titanium alloys *Volume 1: Fundamentals* (New York: Plenum)

[128] Woollam J A and Alterovitz S A 1979 Electronic properties of PbMo$_6$S$_8$ and Cu$_x$Mo$_6$S$_8$ *Phys. Rev.* B **19** 749–61

[129] Ferdeghini C *et al* 2001 Growth of *c*-oriented MgB$_2$ thin films by pulsed laser deposition: structural characterization and electronic anisotropy *Supercond. Sci. Technol.* **14** 952

[130] Kremer R K, Gibson B J and Ahn K 2001 *Heat Capacity of MgB$_2$: Evidence for Moderately Strong Coupling Behaviour* (Los Alamos Server)

[131] Plecenik A, Beňačka Š, Kúš P and Grajcar M 2002 Superconducting gap parameters of MgB$_2$ obtained on MgB$_2$/Ag and MgB$_2$/In junctions *Physica* C **368** 251–4

[132] Poole C P 2000 *Handbook of Superconductivity* 1st edn (New York: Academic)

[133] Ridgeon F J, Raine M J and Hampshire D P 2017 The critical current density of NbTi in the strands used for the ITER poloidal field coils private communication

[134] Cheggour N, Decroux M, Fischer Ø and Hampshire D P 1998 Irreversibility line and granularity in chevrel phase superconducting wires *J. Appl. Phys.* **84** 2181–3